THE JOURNAL OF BIOLOGICAL CHEMISTRY VOL. 289, NO. 50, pp. 34667–34682, December 12, 2014

Crystal Structure of the Middle East Respiratory Syndrome Coronavirus (MERS-CoV) Papain-like Protease Bound to Ubiquitin Facilitates Targeted Disruption of Deubiquitinating Activity to Demonstrate Its Role in Innate Immune Suppression*

Received for publication, September 3, 2014, and in revised form, September 30, 2014 Published, JBC Papers in Press, October 15, 2014, DOI 10.1074/jbc.M114.609644

Ben A. Bailey-Elkin[‡1,2], Robert C. M. Knaap[§2], Garrett G. Johnson[‡], Tim J. Dalebout[§], Dennis K. Ninaber[§], Puck B. van Kasteren[§], Peter J. Bredenbeek[§], Eric J. Snijder[§], Marjolein Kikkert[§3,4], and Brian L. Mark[‡3,5]

From the [‡]Department of Microbiology, University of Manitoba, Winnipeg, Manitoba R3T 2N2, Canada and the [§]Molecular Virology Laboratory, Department of Medical Microbiology, Leiden University Medical Center, 2333 ZA Leiden, The Netherlands

Background: MERS-CoV papain-like protease (PL^{pro}) processes viral polyproteins and has deubiquitinating activity.
Results: A crystal structure of MERS-CoV PL^{pro} bound to ubiquitin guided mutagenesis to disrupt PL^{pro} deubiquitinating activity without affecting polyprotein cleavage.
Conclusion: The deubiquitinating activity of MERS-CoV PL^{pro} suppresses the induction of interferon-β expression.
Significance: Our strategy to selectively disable PL^{pro} deubiquitinating activity enables the study of its specific functions in infection.

Middle East respiratory syndrome coronavirus (MERS-CoV) is a newly emerging human pathogen that was first isolated in 2012. MERS-CoV replication depends in part on a virus-encoded papain-like protease (PL^{pro}) that cleaves the viral replicase polyproteins at three sites releasing non-structural protein 1 (nsp1), nsp2, and nsp3. In addition to this replicative function, MERS-CoV PL^{pro} was recently shown to be a deubiquitinating enzyme (DUB) and to possess deISGylating activity, as previously reported for other coronaviral PL^{pro} domains, including that of severe acute respiratory syndrome coronavirus. These activities have been suggested to suppress host antiviral responses during infection. To understand the molecular basis for ubiquitin (Ub) recognition and deconjugation by MERS-CoV PL^{pro}, we determined its crystal structure in complex with Ub. Guided by this structure, mutations were introduced into PL^{pro} to specifically disrupt Ub binding without affecting viral polyprotein cleavage, as determined using an in *trans* nsp3↓4 cleavage assay. Having developed a strategy to selectively disable PL^{pro} DUB activity, we were able to specifically examine the effects of this activity on the innate immune response. Whereas the wild-type PL^{pro} domain was found to suppress IFN-β promoter activation, PL^{pro} variants specifically lacking DUB activity were no longer able to do so. These findings directly implicate the DUB function of PL^{pro}, and not its proteolytic activity *per se*, in the inhibition of IFN-β promoter activity. The ability to decouple the DUB activity of PL^{pro} from its role in viral polyprotein processing now provides an approach to further dissect the role(s) of PL^{pro} as a viral DUB during MERS-CoV infection.

The Middle East respiratory syndrome coronavirus (MERS-CoV)[6] was first isolated in June 2012 from a patient in Saudi Arabia who had died from progressive respiratory and renal failure (1). Since then, over 800 cases have been reported, with a case fatality rate surpassing 30% (2). The progression and severity of the symptoms observed in MERS patients resemble the severe acute respiratory syndrome (SARS) observed in patients infected with SARS-CoV, which caused a global pandemic in 2003, resulting in over 8000 cases, with a case fatality rate of ~10% (3). Whereas the SARS-CoV outbreak was contained within months, MERS cases continue to occur 2 years after the emergence of MERS-CoV in the human population. Currently, dromedary camels are suspected to be one of the direct reservoirs for the zoonotic transmission of MERS-CoV, although the exact chain of transmission remains to be explored in more detail (4, 5).

MERS-CoV and SARS-CoV are enveloped, positive-sense single-stranded RNA (+RNA) viruses that belong to the *Betacoronavirus* genus in the family Coronaviridae of the Nidovirales order (6). The CoV non-structural proteins (nsps), which

* This work was supported in part by Natural Sciences and Engineering Research Council of Canada Grant 311775-2010 (to B. L. M.), the Division of Chemical Sciences of the Netherlands Organization for Scientific Research (NWO-CW) through ECHO grant 700.59.008 (to M. K. and E. J. S.), and the European Union Seventh Framework Programme (FP7/2007–2013) under SILVER grant agreement 260644.
The atomic coordinates and structure factors (codes 4REZ, 4RF1, and 4RF0) have been deposited in the Protein Data Bank (http://wwpdb.org/).
[1] Recipient of a Research Manitoba Studentship.
[2] Both authors contributed equally to this work.
[3] Both authors contributed equally to this work.
[4] To whom correspondence may be addressed. Tel.: 31-71-526-1442; Fax: 31-71-526-6981; E-mail: m.kikkert@lumc.nl.
[5] Holder of a Manitoba Research Chair award. To whom correspondence may be addressed. Tel.: 204-480-1430; Fax: 204-474-7603; E-mail: brian.mark@umanitoba.ca.

[6] The abbreviations used are: MERS, Middle East respiratory syndrome; CoV, coronavirus; SARS, severe acute respiratory syndrome; nsp, non-structural protein; pp1a and pp1ab, polyprotein 1a and 1ab, respectively; PL^{pro}, papain-like protease; Ub, ubiquitin; DUB, deubiquitinating enzyme; ISG, interferon-stimulated gene; RLR, RIG-I-like receptor; MAVS, mitochondrial antiviral signaling protein; IFN, interferon(s); LSB, Laemmli sample buffer; SUMO, small ubiquitin-like modifier; Ub-3Br, Ub(1–75)-3-bromopropylamine; USP, ubiquitin-specific protease.

drive viral genome replication and subgenomic RNA synthesis, are encoded within a large replicase gene that encompasses the 5′-proximal three-quarters of the CoV genome. The replicase gene contains two open reading frames, ORF1a and ORF1b. Translation of ORF1a yields polyprotein 1a (pp1a), and −1 ribosomal frameshifting facilitates translation of ORF1b to yield pp1ab (7). The pp1a and pp1ab precursors are co- and post-translationally processed into functional nsps by multiple ORF1a-encoded protease domains. CoVs employ either one or two papain-like proteases (PL^{pro}s), depending on the virus species, to release nsp1, nsp2, and nsp3 and a chymotrypsin-like protease (3CL^{pro}) that cleaves all junctions downstream of nsp4 (reviewed in Ref. 8). Comparative sequence analysis of the MERS-CoV genome and proteome allowed for the prediction and annotation of 16 nsps, along with the location of the probable proteolytic cleavage sites (6). The MERS-CoV PL^{pro} domain, which resides in nsp3, has recently been confirmed to recognize and cleave after the sequence L*X*GG at the nsp1 ↓ 2 and nsp2 ↓ 3 junctions, as defined previously for other CoV PL^{pro}s, as well as an LXGG sequence, which constitutes the nsp3 ↓ 4 cleavage site (9, 10).

These recognition sequences within pp1a/pp1ab resemble the C-terminal LRGG motif of ubiquitin (Ub), an 8.5-kDa protein that can be conjugated to lysine residues or the N terminus of target proteins as a form of post-translational modification through the action of the cellular E1/2/3 ligase system (reviewed in Ref. 11). Additional Ub molecules can be linked to any of the 7 lysine residues in Ub itself or to its N terminus to generate polyubiquitin (poly-Ub) chains of various linkage types (11). The best-studied linkages are the ones occurring at Lys^{48} of Ub, which results in the targeting of the tagged substrate to the 26 S proteasome for degradation, and at Lys^{63}, which generates a scaffold for the recruitment of cellular proteins to activate numerous signaling cascades, including critical antiviral and proinflammatory pathways (11). The C terminus of Ub can be recognized by deubiquitinating enzymes (DUBs), which catalyze the deconjugation of Ub, thus reversing the effects of ubiquitination (12). Interestingly, CoV PL^{pro}s, including those of MERS- and SARS-CoV, have been suggested to act as multifunctional proteases that not only cleave the viral polyproteins at internal L*X*GG cleavage sites but also remove Ub and the antiviral Ub-like molecule interferon-stimulated gene 15 (ISG15) from cellular proteins, presumably to suppress host antiviral pathways (9, 13–19).

Activation of antiviral and proinflammatory pathways is a critical first line of defense against virus infections, including those caused by nidoviruses. Viral RNA molecules are recognized by pattern recognition receptors, such as the cytoplasmic RIG-I-like receptors (RLRs) RIG-I and MDA5, which are activated by intracellular viral RNA transcripts bearing 5′ tri- and diphosphates and double-stranded RNA (dsRNA) replication intermediates, respectively (20, 21). Upon their stimulation, RLRs signal through the mitochondrial antiviral signaling protein (MAVS), leading to the formation of a signaling complex at the mitochondrial membrane and ultimately to the activation of transcription factors IRF-3 and NF-κB. These transcription factors in turn regulate the expression of antiviral type 1 interferons (IFN), including IFN-β, which acts through autocrine and paracrine receptor-mediated signaling pathways to induce the transcription of numerous interferon-stimulated genes (ISGs) that will interfere with virus replication as well as proinflammatory cytokines, such as IL-6, IL-8, and TNF-α. Regulation of the antiviral and proinflammatory pathways is largely Ub-dependent, because multiple factors in the innate immune cascade are ubiquitinated, including RIG-I, which is critical for downstream signaling. Cellular DUBs function to prevent excessive inflammation and immune responses during infection by removal of Ub from innate immune factors (reviewed in Ref. 22).

The DUB activities of MERS- and SARS-CoV PL^{pro} have been implicated in the suppression of host antiviral pathways because these proteases can suppress IFN-β induction upon their ectopic expression (9, 13, 15, 16, 19, 23). Previous work has shown that during infection, SARS-CoV indeed suppresses the host's antiviral responses by preventing the induction of IFN-β expression in cell culture (24–26). Similarly, MERS-CoV infection has been found to elicit a poor type-1 IFN response in cultured monocyte-derived dendritic cells (27) and alveolar epithelial A549 cells (28) as well as *ex vivo* in bronchial and lung tissue samples (28). Furthermore, delayed induction of proinflammatory cytokines in human airway epithelial cells infected with MERS-CoV has been reported (29).

Although the above observations suggest that MERS- and SARS-CoV actively suppress antiviral responses, such as IFN-β production and inflammation, they do not directly implicate the DUB activity of PL^{pro} as being responsible for (part of) this suppression. Due to the dependence of MERS-CoV replication on the ability of PL^{pro} to cleave the nsp1–nsp3 region of the replicase polyproteins, studying the role of PL^{pro} DUB activity, specifically in the suppression of the cellular innate immune response, is difficult because both activities depend on the same enzyme active site. Selective inactivation of only the DUB activity of PL^{pro} would enable the study of how this activity alone affects cellular signaling; however, achieving this requires detailed information on the structural basis of Ub recognition and deconjugation by PL^{pro}. To this end, we determined the crystal structure of MERS-CoV PL^{pro} bound to Ub to elucidate the molecular determinants of Ub recognition. Based on the structure of this complex, mutations were introduced that selectively disrupted Ub recognition by targeting regions of the Ub-binding site on PL^{pro} that were sufficiently distant from the active site of the protease. Using this approach, we were able to remove the DUB activity from PL^{pro} without affecting its ability to cleave the nsp3 ↓ 4 cleavage site *in trans*. This enabled us, for the first time, to demonstrate that the DUB activity of MERS-CoV PL^{pro} can suppress the MAVS-mediated induction of IFN-β expression.

EXPERIMENTAL PROCEDURES

Cells, Antibodies, and Plasmids—HEK293T cells were cultured in Dulbecco's modified Eagle's medium (DMEM) supplemented with 10% fetal calf serum (FCS; Bodinco BV), 100 units/ml penicillin, 100 units/ml streptomycin, and 2 mM L-glutamine (cell culture medium and supplements were obtained from Lonza).

Primary antibodies used were mouse anti-HA (ab18181; Abcam), mouse anti-V5 (37-7500; Invitrogen), mouse anti-β-actin (A5316; Sigma-Aldrich), mouse anti-FLAG (F3165;

Sigma-Aldrich), and rabbit anti-GFP (30). As secondary antibodies, horseradish peroxidase (HRP)-conjugated antibodies were used (P0447 and P0217; Dako).

The following plasmids were described elsewhere: pASK3 (31), pcDNA-eGFP (30), pCMV-FLAG-Ub (32), pLuc-IFN-β (33), pEBG-RIG-$I_{(2CARD)}$ (34), pcDNA-FLAG-MAVS (35), and pEGFP-C1-$IRF3_{(5D)}$ (36).

Construction of MERS-CoV PL^{pro} Expression Plasmids—A cDNA fragment encoding the PL^{pro} domain (amino acids 1479–1803 of the MERS-CoV pp1a/pp1ab polyprotein (NCBI ID: JX869059); pp1a/pp1ab amino acid numbering is used throughout the rest of this work) was cloned into bacterial expression vector pASK3 in-frame with N-terminal Ub and a C-terminal His_6 purification tag to produce pASK-MERS-CoV-PL^{pro}.

Using standard methodologies, the sequence encoding amino acids 1480–1803 of MERS-CoV pp1a/pp1ab was PCR-amplified, cloned downstream of the T7 promoter of expression vector pE-SUMO (LifeSensors), and used to transform *Escherichia coli* BL21 (DE3) GOLD cells (Stratagene) grown under kanamycin selection (35 μg/ml). Recombinant expression plasmid (pE-SUMO-PL^{pro}) was isolated from a single colony, and DNA sequencing confirmed the expected sequence of the PL^{pro} domain and the in-frame fusion of the 5′-end to a sequence encoding a His_6-SUMO purification tag, which facilitated purification of the product by immobilized metal (nickel) affinity chromatography as described below.

To obtain high expression in eukaryotic cells, the sequence of MERS-CoV nsp3–4 (amino acids 854–3246) flanked by an N-terminal HA tag and a C-terminal V5 tag was optimized based on the human codon usage frequency, and potential splice sites and polyadenylation signals were removed. This sequence was synthesized (Invitrogen) and subsequently cloned into the pCAGGS vector (Addgene) using standard methodologies. The following expression constructs were generated: pCAGGS-HA-nsp3-4-V5 (amino acids 854–3246), pCAGGS-HA-nsp3C-4-V5 (amino acids 1820–3246, which does not include the PL^{pro} domain), and pCAGGS-HA-nsp3-Myc (amino acids 854–2739). The sequence encoding MERS-CoV PL^{pro} (amino acids 1479–1803) was PCR-amplified using synthetic plasmid DNA as a template and cloned in frame with a C-terminal V5 tag in the pcDNA3.1(−) vector (Invitrogen). The pASK-MERS-CoV-PL^{pro} and pcDNA3.1-MERS-CoV-PL^{pro} expression constructs served as templates for site-directed mutagenesis using the QuikChange strategy with *Pfu* DNA polymerase (Agilent). All constructs were verified by sequencing. The sequences of the constructs and primers used in this study are available upon request.

Purification of MERS-CoV PL^{pro} and in Vitro DUB Activity Assay—In vitro DUB activity assays were performed with recombinant MERS-CoV PL^{pro} batch-purified from lysates of *E. coli* strain C2523. Cells transformed with pASK-MERS-CoV-PL^{pro} were cultured to an A_{600} of 0.6 in lysogeny broth at 37 °C. Protein expression was then induced with 200 ng/ml anhydrotetracycline for 16 h at 20 °C. The cells were pelleted, resuspended in lysis buffer (20 mM HEPES, pH 7.0, 200 mM NaCl, 10% (v/v) glycerol, and 0.1 mg/ml lysozyme), and lysed for 1 h at 4 °C, followed by sonication. The lysate was clarified by centrifugation at 20,000 × *g* for 20 min at 4 °C, and the soluble fraction was applied to Talon resin (GE Healthcare) pre-equilibrated with lysis buffer. After a 2-h rolling incubation at 4 °C, the beads were washed four times with wash buffer (20 mM HEPES, pH 7.0, 200 mM NaCl, 10% (v/v) glycerol, and 20 mM imidazole), followed by the elution of the protein with elution buffer (20 mM HEPES, pH 7.0, 200 mM NaCl, 10% (v/v) glycerol, and 250 mM imidazole). Eluted protein was dialyzed against storage buffer (20 mM HEPES, pH 7.0, 100 mM NaCl, 50% (v/v) glycerol, 2 mM dithiothreitol (DTT)) and stored at −80 °C. N-terminal Ub is cleaved from the Ub-PL^{pro}-His_6 fusion protein by the PL^{pro} domain itself during expression. To achieve removal of the Ub from mutated and/or inactive PL^{pro}, *E. coli* strain C2523 containing pCG1, expressing the ubiquitin-specific processing protease 1 (Ubp1), was used (37).

In vitro DUB activity assays were performed as described by van Kasteren *et al.* (30). Briefly, the indicated amounts of purified MERS-CoV PL^{pro} wild type or active site mutant (C1592A) were incubated with 2.5 μg of either Lys^{48}-linked poly-Ub chains or Lys^{63}-linked poly-Ub chains (Boston Biochem) in a final volume of 10 μl. Isopeptidase T (Boston Biochem) served as a positive control. After a 2-h incubation at 37 °C, the reaction was stopped by the addition of 4× Laemmli sample buffer (4× LSB; 500 mM Tris, 4% SDS, 40% glycerol, 0.02% bromphenol blue, 2 mM DTT, pH 6.8). SDS-polyacrylamide gels were stained with Coomassie Brilliant Blue (Sigma-Aldrich) and scanned using a GS-800 calibrated densitometer (Bio-Rad).

Expression and Purification of MERS-CoV PL^{pro} for Crystallization—E. coli BL21(DE3) GOLD cells harboring pE-SUMO-PL^{pro} were grown at 37 °C with aeration in 500 ml of lysogeny broth containing kanamycin (35 μg/ml) to an A_{600} of 0.6–0.8. Expression of the His_6-SUMO-PL^{pro} fusion protein was then induced by the addition 1 mM isopropyl β-D-1-thiogalactopyranoside for 18 h at 16 °C with aeration. Cells were pelleted by centrifugation and stored at −80 °C.

Cell pellets were resuspended in ice-cold lysis buffer (150 mM Tris, pH 8.5, 1 M NaCl, 0.1 mM phenylmethanesulfonyl fluoride (PMSF), 2 mM DTT) and lysed using a French pressure cell (AMINCO). Cell lysate was clarified by centrifugation (17,211 × *g* at 4 °C), and the supernatant containing the His_6-SUMO-PL^{pro} fusion was applied to a column containing nickel-nitrilotriacetic acid affinity resin (Qiagen). The column was washed with 10 column volumes of lysis buffer supplemented with 25 mM imidazole, followed by elution of the fusion protein with lysis buffer containing 250 mM imidazole. The His_6-SUMO tag was then removed from PL^{pro} by adding His_6-tagged Ulp1 SUMO protease to the eluted SUMO-PL^{pro} fusion, followed by dialysis of the protein mixture overnight against 2 liters of cleavage buffer (150 mM NaCl, 50 mM Tris, pH 8.0, 1 mM DTT) at 4 °C. Tag-free PL^{pro} was separated from His_6-SUMO and the His_6-Ulp1 SUMO protease by passing the dialyzed protein mix through a nickel-nitrilotriacetic acid gravity column. The flow-through contained purified PL^{pro} that was subsequently dialyzed against 20 mM Tris, pH 8.5, 150 mM NaCl, 2 mM DTT and further purified by gel filtration using a Superdex 75 (GE Healthcare) gel filtration column.

Covalent Coupling of Ub to PL^{pro}—Ub(1–75)-3-bromopropylamine (Ub-3Br) is a modified form of Ub with a reactive C

TABLE 1
Crystallographic statistics for MERS-CoV PL^{pro} and PL^{pro}·Ub structures

Crystal	PL^{pro}	Open PL^{pro}·Ub	Closed PL^{pro}·Ub
Crystal geometry			
Space group	$P6_3$	$P6_3$	$P6_522$
Unit cell (Å)	$a = b = 137.94$ $c = 57.70$; $\alpha = \beta = 90°$ $\gamma = 120°$	$a = b = 136.77$ $c = 57.99$; $\alpha = \beta = 90°$ $\gamma = 120°$	$a = b = 176.92$ $c = 84.55$; $\alpha = \beta = 90°$ $\gamma = 120°$
Crystallographic data			
Wavelength (Å)	1.28294	1.28280	1.28219
Resolution range (Å)	45.15–2.60 (2.90–2.80)[a]	44.23–2.15 (2.22–2.15)	44.24–2.60 (2.90–2.80)
Total observations	137,170 (13,780)	124,058 (12,315)	283,649 (28,118)
Unique reflections	15,683 (1566)	33,472 (3291)	19,694 (1918)
Multiplicity	8.7 (8.8)	3.7 (3.7)	14.4 (14.7)
Completeness (%)	100.00 (100.00)	98.73 (98.12)	99.97 (100)
Anomalous completeness	99.4 (98.5)	92.4 (92.6)	100 (100)
R_{merge}	0.085 (0.76)	0.041 (0.79)	0.061 (0.78)
CC1/2	0.99 (0.83)	0.99 (0.54)	1 (0.93)
CC*	0.99 (0.95)	1 (0.84)	1 (0.98)
$I/\sigma I$	17.13 (3.42)	20.52 (1.97)	34.01 (3.69)
Wilson *B*-factor (Å^2)	75.15	46.79	74.96
Phasing statistics			
Figure of merit	0.12	0.18	0.23
Figure of merit after RESOLVE	0.64	0.63	0.67
Refinement statistics			
Reflections in test set	1570	1996	1609
Protein atoms	2384	3020	3020
Zinc atoms	1	1	1
Solvent molecules	26	205	65
R_{work} (R_{free})	0.23 (0.27)	0.20 (0.23)	0.24 (0.28)
Root mean square deviations			
Bond lengths/angles (Å/degrees)	0.002/0.60	0.002/0.52	0.002/0.54
Ramachandran plot			
Favored/allowed (%)	95/5	95/5	93/7
Average *B*-factor (Å^2)	76.70	66.80	86.50
B-Factor for macromolecules	76.70	69.20	86.60
B-Factor for solvent	76.65	65.40	84.20

[a] Values in parentheses refer to the highest resolution shell.

terminus that forms an irreversible covalent linkage to the active site cysteine of DUBs and was prepared according to Messick *et al.* (38) and Borodovsky *et al.* (39). Purified PL^{pro} was incubated with a 2-fold molar excess of Ub-3Br and incubated for 1 h at room temperature with end-over-end mixing. The resulting PL^{pro}·Ub complex was dialyzed into 20 mM Tris, pH 8.5, 150 mM NaCl, 2 mM DTT, and excess Ub-3Br was removed by gel filtration using a Superdex 75 column.

Crystallization of PL^{pro} and PL^{pro}·Ub Complexes—The purified PL^{pro}·Ub complex was concentrated and crystallized at 20 °C in two different conditions using the vapor diffusion method: 1) 20% PEG 4000, 0.1 M trisodium citrate, pH 5.4, 20% isopropyl alcohol at 10 mg/ml, which yielded the structure of open PL^{pro}·Ub (see "Results"), and 2) 1.80 M ammonium sulfate ($AmSO_4$) at 20 mg/ml, which yielded the structure of closed PL^{pro}·Ub (see "Results"). Crystals of unliganded PL^{pro} were also grown using the vapor diffusion method in 18% PEG 4000, 0.1 M trisodium citrate, pH 5.6, 16% isopropyl alcohol after concentrating the protein to 12 mg/ml. Immediately prior to crystallization, 1 M DTT was added to the protein to a final concentration of 5 mM, which was found to improve crystallization.

In preparation for x-ray data collection, single crystals of open PL^{pro}·Ub from condition 1 above were briefly swept through a droplet of cryoprotectant composed of 22% PEG 4000, 0.1 M trisodium citrate, pH 5.6, 20% 1,2-propanediol before flash cooling in liquid nitrogen. Similarly, single crystals of closed PL^{pro}·Ub from condition 2 above and unbound PL^{pro} were cryoprotected in 1.85 M $AmSO_4$, 15% glycerol and 22% PEG 4000, 0.1 M trisodium citrate, pH 5.6, 10% 1,2-propanediol, respectively, before flash cooling in liquid nitrogen.

Data Collection and Structure Determination—X-ray diffraction data were collected from all crystals at the Zn-K absorption edge at beamline 08B1-1 of the Canadian Light Source and integrated using XDS (40). Integrated data were then scaled using Scala (41). Initial phase estimates for reflections collected from unliganded and Ub-bound PL^{pro} were determined via a single wavelength anomalous dispersion experiment. The position of the zinc anomalous scatterer was identified using HySS (42), and density modification was performed with RESOLVE (43) within the phenix.autosol pipeline (44). Initial models were constructed using phenix.autobuild, and further model building and refinement were carried out using Coot (45) and phenix.refine (46). Crystallographic statistics for all structures are found in Table 1.

Protease Activity Assays in Cell Culture—HEK293T cells, grown to 80% confluence in 12-well plates, were transfected using the calcium phosphate transfection method (47). To determine the DUB activity of MERS-CoV PL^{pro}, plasmids encoding FLAG-tagged Ub (0.25 μg), GFP (0.25 μg), and MERS-CoV-PL^{pro}-V5 (0.2 μg) were co-transfected. A combination of plasmids encoding GFP (0.25 μg), HA-nsp3C-4-V5 (0.2 μg), and MERS-CoV-PL^{pro}-V5 (0.15 μg) were transfected to assess the in *trans* cleavage activity of MERS-CoV-PL^{pro}. Total amounts of transfected DNA were equalized to 2 μg by the addition of empty pcDNA vector. At 18 h post-transfection, cells were lysed in 2× LSB. Proteins were separated in an SDS-

polyacrylamide gel and blotted onto Hybond-P (GE Healthcare) using the Trans-blot turbo transfer system (Bio-Rad). Aspecific binding to the membrane was blocked with dried milk powder solution, and after antibody incubation, protein bands were visualized using Pierce ECL 2 Western blotting substrate (Thermo Scientific).

Luciferase-based IFN-β Reporter Assay—Using the calcium phosphate method, 80% confluent HEK293T cells in 24-well plates were transfected with 5 ng of plasmid pRL-TK (Promega) encoding *Renilla* luciferase; IFN-β-Luc firefly reporter plasmid (25 ng); innate immune response inducer plasmids encoding RIG-I$_{(2CARD)}$, MAVS, or IRF3$_{(5D)}$ (25 ng); and the indicated quantities of MERS-CoV PL^{pro}- or MERS-CoV nsp3-encoding expression plasmids. Total amounts of transfected DNA were equalized to 1 μg by the addition of empty pcDNA vector. At 16 h post-transfection, cells were lysed in 1× passive lysis buffer (Promega). Firefly and *Renilla* luciferase activity was measured using the Dual-Luciferase reporter assay system (Promega) on a Mithras LB 940 multimode reader (Berthold Technologies). Experiments were performed in triplicate and independently repeated at least four times. Firefly luciferase activity was normalized to *Renilla* luciferase, and statistical significance was determined using an unpaired two-tailed Student's *t* test. Values of <0.05 were considered statistically significant. 4× LSB was added to the remaining lysates, and these samples were analyzed by Western blotting as described above.

RESULTS

DUB Activity of Recombinant MERS-CoV PL^{pro}

It was recently shown in cell culture experiments that ectopic expression of MERS-CoV PL^{pro} resulted in deconjugation of poly-Ub and ISG15 from cellular targets (9, 16). DUB activity of purified recombinant MERS-CoV PL^{pro} was also demonstrated using Ub-7-amino-4-trifluoromethylcoumarin (48) or Ub-7-amino-4-methylcoumarin (49) as a substrate. To characterize the direct activity of recombinant MERS-CoV PL^{pro} toward poly-Ub, we purified the enzyme from *E. coli* and incubated it with either Lys^{48}- or Lys^{63}-linked poly-Ub chains. Wild-type PL^{pro} degraded both Lys^{48}- and Lys^{63}-linked chains in a concentration-dependent manner, whereas mutating the active site nucleophile (C1592A) severely reduced the activity of the enzyme toward both Ub linkage types (Fig. 1). No clear preference of the enzyme for cleaving either the Lys^{63} or the Lys^{48} Ub linkage was observed under the conditions used in this *in vitro* DUB assay (Fig. 1, compare *A* and *B*). This assay clearly demonstrated that the protease domain used throughout this study for ectopic expression and crystallization experiments possesses DUB activity toward Lys^{48}- and Lys^{63}-linked Ub chains and that this activity does not require other viral or cellular proteins. During the preparation of this manuscript, an article by Báez-Santos *et al.* (50) was published in which similar results were presented.

Crystal Structures of MERS-CoV PL^{pro} and PL^{pro}·Ub Complexes

MERS-CoV PL^{pro}—The crystal structure of PL^{pro} was determined both on its own and as a covalent complex with Ub (PL^{pro}·Ub). The PL^{pro} domain crystallized in space group P6$_3$, and consistent with another recently determined crystal structure of MERS-CoV PL^{pro} (49), we found the protease to

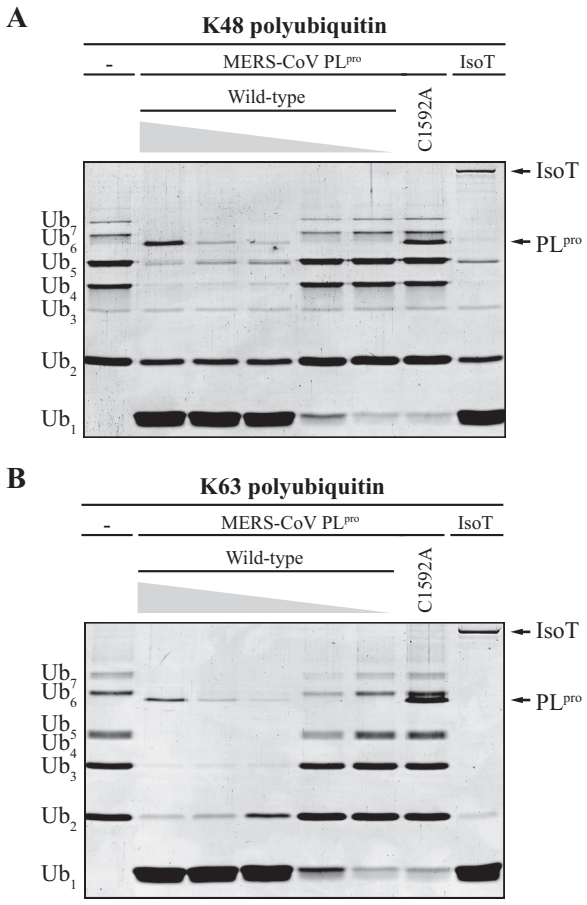

FIGURE 1. ***In vitro* cleavage of Lys^{48}- and Lys^{63}-linked poly-Ub chains by recombinant MERS-CoV PL^{pro}.** Purified recombinant MERS-CoV PL^{pro} was incubated with 2.5 μg of Lys^{48}-linked (*A*) or Lys^{63}-linked (*B*) poly-Ub chains of different length in each reaction for 2 h at 37 °C in a final volume of 10 μl. A range of 2-fold dilutions starting at 2 μM MERS-CoV wild-type PL^{pro} per reaction was used. Activity of the PL^{pro} active site mutant (C1592A) was assessed at a concentration of 2 μM. Isopeptidase T (*IsoT*; 0.5 μg/reaction) served as a positive control (69).

adopt a fold consistent with DUBs of the ubiquitin-specific protease (USP) family. The structure includes a C-terminal catalytic domain containing a right-handed fingers, palm, and thumb domain organization as well as an N-terminal Ub-like (Ubl) domain found in many USPs, including that of SARS-CoV (51, 52) (Fig. 2*A*). The packing of the palm and thumb domains forms a cleft leading into the active site in a manner consistent with the domain organization prototyped by the Clan CA group of cysteine proteases (53). The Ubl domain packs against the thumb domain composed of helices α2–7, which in turn packs against the palm domain composed of strands β6, β7, and β14–19. Extending from the palm, the fingers domain is composed of strands β10, β11, β13, β14, and β19 and contains a C$_4$ zinc ribbon motif (54) coordinating a zinc atom via residues Cys^{1672}, Cys^{1675}, Cys^{1707}, and Cys^{1709} in tetrahedral geometry, similar to that of SARS PL^{pro}, transmissible gastroenteritis coronavirus PL1^{pro}, and cellular USP2 and USP21 (51, 55–57).

PL^{pro} Covalently Bound to Ub—The MERS-CoV PL^{pro}·Ub complex crystallized in two different space groups (P6$_3$ and P6$_5$22), which revealed a considerable level of conformational flexibility in the protein. Electron density maps calculated using diffraction data collected from PL^{pro}·Ub complex that crystal-

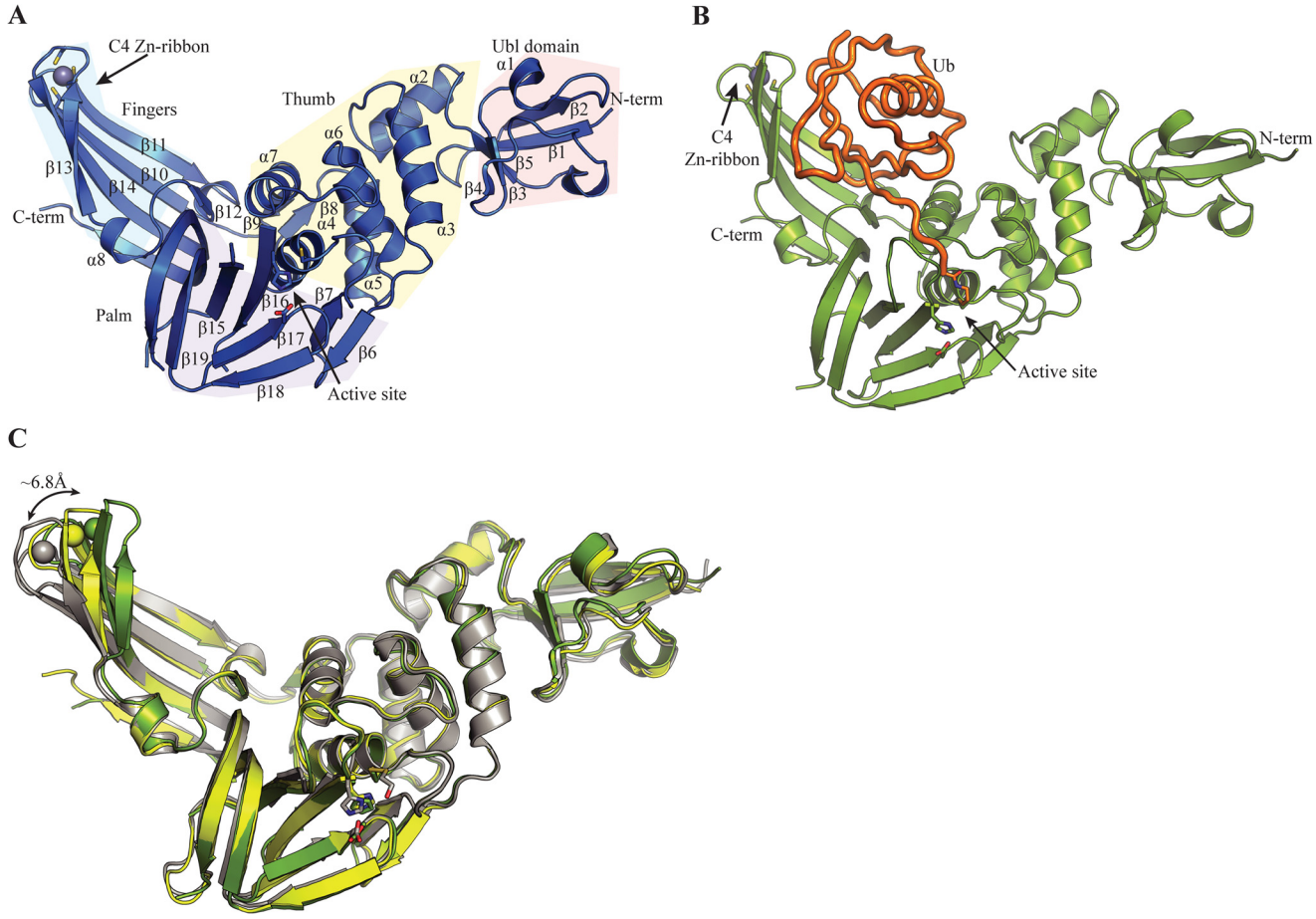

FIGURE 2. **MERS-CoV PL^{pro} and PL^{pro}·Ub structures.** *A*, structure of the MERS-CoV PL^{pro} domain (2.15 Å resolution). The palm, thumb, fingers, and N-terminal ubiquitin-like (Ubl) domains are indicated by *colored panels*, and *arrows* indicate the active site and C_4 zinc ribbon motif. The active site residues are depicted as *sticks*. *B*, structure of the MERS-CoV PL^{pro} bound to Ub (2.8 Å resolution). PL^{pro} is shown in *green*, and the covalently bound Ub molecule is *orange* and shown as *tubes*. Active site residues are shown as *sticks* with Gly^{75} and the 3CN linker of Ub covalently linked to Cys^{1592} of PL^{pro}. *C*, superposition showing a ~6.8-Å movement of the zinc ribbon motif between the open (*yellow*) and closed (*green*) PL^{pro}·Ub structures and a previously reported PL^{pro} structure (*gray*) (Protein Data Bank entry 4P16 (49)). Our PL^{pro} structure is not shown because it is highly similar to the open PL^{pro}·Ub structure. Movement of the zinc ribbon motif was determined by measuring the distance between the zinc atom of the respective structures. Superpositions were performed in Coot (45). Ub was removed from the closed and open PL^{pro}·Ub structures for clarity. Figures were created using PyMOL (70).

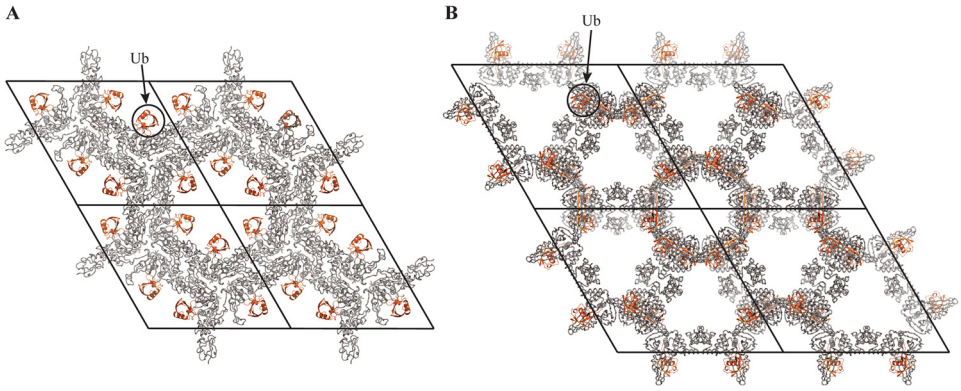

FIGURE 3. **Crystal packing arrangement of the open and closed MERS-CoV PL^{pro}·Ub structures.** The contents of four unit cells are shown, with PL^{pro} and Ub depicted in *gray* and *orange*, respectively. *A*, the open PL^{pro}·Ub structure crystallized in space group $P6_3$, where Ub was found to face the solvent, uninvolved in crystal contacts. *B*, the closed PL^{pro}·Ub structure crystallized in space group $P6_522$, where Ub no longer faces the solvent, and is involved in crystal contacts. Images were created using PyMOL (70).

lized in space group $P6_3$ revealed weak density for the covalently bound Ub molecule. Although the entire bound Ub molecule could be modeled within its binding site on PL^{pro} in this crystal form, high temperature factors for atoms comprising the modeled Ub molecule suggested that it was not rigidly bound to the protease despite being covalently linked to the active site cysteine. Further analysis of the crystal packing revealed that the Ub molecule was fully exposed to solvent and not involved in crystal contacts, which provided a degree of mobility to Ub when bound to PL^{pro} (Fig. 3*A*). This result

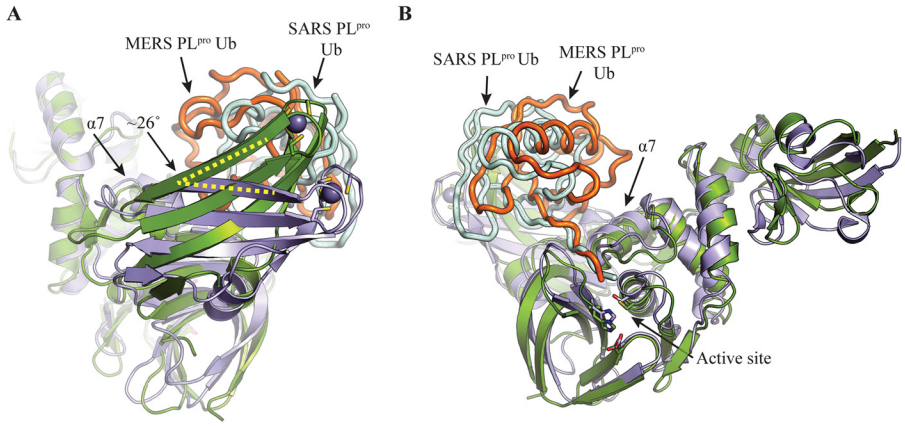

FIGURE 4. **Structural comparison of the SARS-CoV PL^{pro}·Ub and MERS-CoV PL^{pro}·Ub complexes.** *A*, superposition of the closed MERS-CoV PL^{pro}·Ub complex (*green*) and the SARS-CoV PL^{pro}·Ub complex (*purple*; Protein Data Bank entry 4M0W) using SSM superpose in Coot (45) (bound Ub molecules were ignored during the superposition). The Ub molecules bound to the MERS-CoV PL^{pro} domain and SARS-CoV PL^{pro} domain are depicted as *tubes* in *orange* and *pale cyan*, respectively. The ~26° shift in the fingers domain between the two respective structures is indicated. *B*, alternate orientation of the SARS-CoV PL^{pro}·Ub and MERS-CoV PL^{pro}·Ub superpositions highlighting the difference in Ub binding. In the MERS-CoV PL^{pro}·Ub complex, Ub is found shifted toward helix α7 compared with the SARS PL^{pro}·Ub complex. Helix α7 of MERS-CoV PL^{pro} is indicated with an *arrow*. Images were created using PyMOL (70).

encouraged us to pursue additional crystallization conditions, which yielded crystals of PL^{pro}·Ub in space group P6$_5$22 (Figs. 2*B* and 3*B*). The crystal packing in this space group allowed for multiple crystal contacts between the bound Ub monomer and surrounding symmetry mates and resulted in clear, well defined density for the Ub molecule (Fig. 3*B*). Interestingly, relative to the P6$_3$ crystal forms of PL^{pro}, the fingers domain in this crystal form was moved toward Ub (Fig. 2*C*). In light of these movements, the PL^{pro}·Ub structure with the fingers domain positioned away from Ub (space group P6$_3$) will hereafter be referred to as "open" PL^{pro}·Ub, whereas the structure with the fingers domain shifted toward Ub (space group P6$_5$22) will be referred to as "closed" PL^{pro}·Ub. An overlay of the different PL^{pro} crystal structures that have been determined reveals that these structures vary in the position of the zinc ribbon motif, further suggesting a high degree of mobility for this region (Fig. 2*C*). In line with this observation, movement of the fingers domain toward bound Ub was also reported for the SARS-CoV PL^{pro} domain, which displayed a 3.8-Å movement of the zinc atom when comparing the Ub-bound and unbound structures (58). Further comparison of the closed MERS-CoV PL^{pro}·Ub structure with the recently determined SARS-CoV PL^{pro}·Ub structure (58) revealed differences in the relative orientation of the fingers domain of the two proteases. The MERS-CoV PL^{pro} fingers domain was found to be shifted ~26° away from the palm domain compared with that of SARS-CoV PL^{pro}, resulting in a slight difference in the Ub binding orientation, with the MERS-CoV PL^{pro}-bound Ub being positioned closer toward helix α7 of the palm domain (Fig. 4).

PL^{pro} Active Site Organization and Interaction with the C-terminal RLRGG Motif of Ub

The cleft formed between the palm and thumb domains of PL^{pro} guides the C-terminal ^{72}RLRGG^{76} motif of Ub toward the protease active site, and the interactions between the C-terminal motif of Ub and the active site cleft are depicted in Fig. 5 (*A* and *B*). The PL^{pro} active site is composed of a Cys^{1592}-His^{1759}-Asp^{1774} catalytic triad, which adopts a catalytically competent arrangement in both the unliganded and Ub-bound structures of PL^{pro} (Fig. 5*C*). The oxyanion hole of the PL^{pro} active site appears to be composed of backbone amides from residues Asn^{1590}, Asn^{1591}, and Cys^{1592}, which appear suitably arranged to stabilize the negative charge that develops on the carbonyl oxygen of the scissile bond during catalysis (Fig. 5*C*). Interestingly, as noted by Lei *et al.* (49), the MERS-CoV PL^{pro} active site appears incomplete. In SARS-CoV PL^{pro}, Trp^{107} (amino acid numbering according to the structure of Protein Data Bank entry 2FE8) is positioned within the enzyme's active site with the indole nitrogen of its side chain oriented such that it is probably involved in forming part of the oxyanion hole (51). In the case of MERS-CoV PL^{pro}, we and others (48, 49) have found the structurally equivalent residue in MERS-CoV PL^{pro} to be Leu^{1587}, which would be unable to participate in stabilizing the oxyanion during catalysis. Furthermore, it was recently shown that MERS-CoV PL^{pro} L1587W mutants show greater catalytic efficiency than wild-type PL^{pro} (48, 49). Given the effect this residue has on the catalytic rate of PL^{pro}, it will be very interesting to understand how this residue influences MERS-CoV replication kinetics. It has been proposed that the decreased catalytic efficiency may influence maturation of the MERS-CoV polyprotein (48) and could be involved in the recognition of residues downstream of the scissile bond of the polyprotein cleavage sites or in the modulation of PL^{pro} DUB activity.

Interestingly, differences were observed in the position of a loop on PL^{pro} connecting strands β15 and β16, which is structurally analogous to the blocking loop (BL2) first described in the structure of USP14 (59). This loop is disordered in our unliganded PL^{pro} structure and that previously determined by others (49); however, in both of our PL^{pro}·Ub structures, we found this loop to be fully resolved, supported by the main-chain hydrogen-bonding interactions between Arg^{74} of Ub and Gly^{1758} of PL^{pro}, as well as a hydrophobic interaction between Val^{1757} and Pro^{1644}, two PL^{pro} residues present on opposite sides of the active site cleft (Fig. 5*A*). The side-chain η-amino group of the Ub residue Arg^{74} is also hydrogen-bonded to the main-chain carbonyl group of PL^{pro} residue Thr^{1755}; however, this interaction is only seen in the open PL^{pro}·Ub structure. The

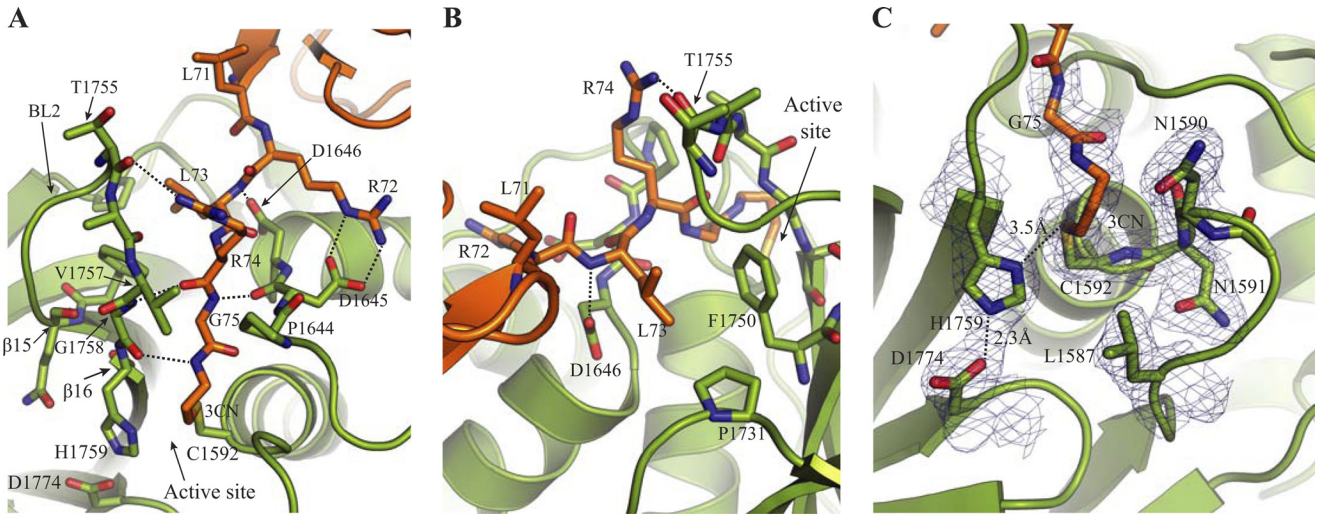

FIGURE 5. **Active site of MERS-CoV PL^{pro} and interactions with the C-terminal RLRGG motif of Ub.** Interactions between open PL^{pro} (*green*) and the C-terminal RLRGG motif of Ub (*orange*) are depicted in *A* and *B*. *A*, the main-chain amide of the 3CN linker, which mimics Gly^{76} of Ub, forms a hydrogen bond with the main chain carbonyl of PL^{pro} residue Gly^{1758}. The main-chain amide of Gly^{75} of Ub forms a hydrogen bond with the carbonyl group of PL^{pro} Asp^{1645}, and a hydrogen bonding interaction occurs between the main-chain carbonyl of Arg^{74} of Ub and the main-chain amide of Gly^{1758} of PL^{pro}. The side-chain η-amino group of Ub residue Arg^{74} is hydrogen-bonded to the main-chain carbonyl group of PL^{pro} Thr^{1755}. Hydrogen bonds also occur between the side-chain ϵ- and η-amino groups of Ub Arg^{72} and the carboxylate of PL^{pro} Asp^{1645} as well as between the main-chain amide of Ub residue Leu^{73} and side chain PL^{pro} residue Asp^{1646}. The BL2 loop between strands β15 and β16 is indicated with an *arrow*. *B*, alternate orientation of the PL^{pro} active site showing a hydrogen bonding interaction between the Ub Leu^{73} main-chain amide group and the side-chain carboxylate of PL^{pro} residue Asp^{1646}. The side chain of Ub residue Leu^{63} also undergoes hydrophobic interactions with PL^{pro} residues Phe^{1750} and Pro^{1731}. *C*, the MERS-CoV PL^{pro} Cys^{1592}-His^{1759}-Asp^{1774} catalytic triad residues are shown as well as residues Asn^{1590} and Asn^{1591}, which together with Cys^{1592} form the oxyanion hole via their backbone amide groups. The covalent 3CN molecule is shown linking the C terminus of Ub to the active site Cys^{1592} of PL^{pro}. The active site Leu^{1587} residue, which is not involved in oxyanion hole formation, is also shown. The electron density is a maximum likelihood weighted $2F_o - F_c$ map contoured at 1.0σ. Images were created using PyMOL (70).

SARS-CoV PL^{pro} domain has also been crystallized both in the presence (51) and absence (58) of Ub, and although the BL2 loop of unbound SARS-CoV PL^{pro} was resolved in two of three monomers of the asymmetric unit, the third showed weak electron density for BL2 and high temperature factors, indicating a high degree of mobility. In addition, in the transmissible gastroenteritis coronavirus USP domain PL1^{pro}, a structurally analogous BL2 loop was found to be in an open conformation with poorly defined electron density in the absence of substrate (55). It is interesting to note that all three coronavirus USP DUBs crystallized to date (from MERS-CoV, SARS-CoV, and transmissible gastroenteritis coronavirus) demonstrate a significant degree of flexibility within the BL2 loop region in the absence of substrate and that none of the structures determined in their unbound form demonstrate obstruction of the active site via BL2.

Structure-guided Design of PL^{pro} Mutants Defective in DUB Activity

We previously demonstrated that the DUB activity of the papain-like protease 2 (PLP2) from equine arteritis virus (another member of the nidovirus order), which resembles the ovarian tumor (OTU) domain-containing family of DUBs (60), could be selectively removed without affecting its ability to process the equine arteritis virus replicase polyprotein. This allowed us to establish that the DUB activity of PLP2 is directly responsible for suppressing Ub-dependent antiviral pathways during infection of primary host cells (61). Subsequently, Ratia *et al.* (62) applied a similar strategy to the SARS-CoV PL^{pro} domain in order to partially remove the DUB activity of PL^{pro} while maintaining the nsp2-3-processing function. We now used the crystal structure of the USP-like MERS PL^{pro}·Ub complex to guide the design of mutations targeting the Ub-binding site on PL^{pro} that would completely disrupt Ub binding without affecting the structural integrity of the active site. PL^{pro} residues interacting directly with Ub were replaced with larger, bulkier residues that would prevent Ub binding by altering both shape and surface electrostatics of the Ub-binding site. Individual mutation of eight different PL^{pro} residues (Arg^{1649}, Thr^{1653}, Ala^{1656}, Asn^{1673}, Val^{1674}, Val^{1691}, Val^{1706}, and Gln^{1708}) and combinations thereof were generated (Fig. 6, *A–D*). Importantly, these residues are located at a distance from the PL^{pro} active site, and thus we hypothesized that they would only participate in DUB activity and not polyprotein processing.

Despite significant movement within the fingers domain of PL^{pro}, most interactions between the protease and Ub are consistent between the open and closed Ub-bound complexes. Residue Ile^{44} of Ub, which forms part of the hydrophobic patch that is commonly recognized by Ub-binding proteins (63), interacts with the hydrophobic side chain of Val^{1691} of PL^{pro} (Fig. 6*B*). Residues Gln^{49} and Glu^{51} of Ub form hydrogen-bonding interactions with Thr^{1653} that is present on helix α7, which runs through the center of PL^{pro}. Two arginine residues, Arg^{1649} of PL^{pro} and Arg^{72} of Ub (the latter of which forms part of the C-terminal tail of Ub that is bound in the PL^{pro} active site cleft) are oriented such that the guanidinium groups of these residues are arranged in a stacked conformation (Fig. 6*C*). In addition, due to the inward movement toward Ub of the closed PL^{pro}·Ub fingers domain, a unique hydrogen-bonding interaction between Gln^{62} of Ub and Gln^{1708} of PL^{pro} and a hydrophobic interaction between Phe^{4} of Ub and Val^{1706} of PL^{pro}

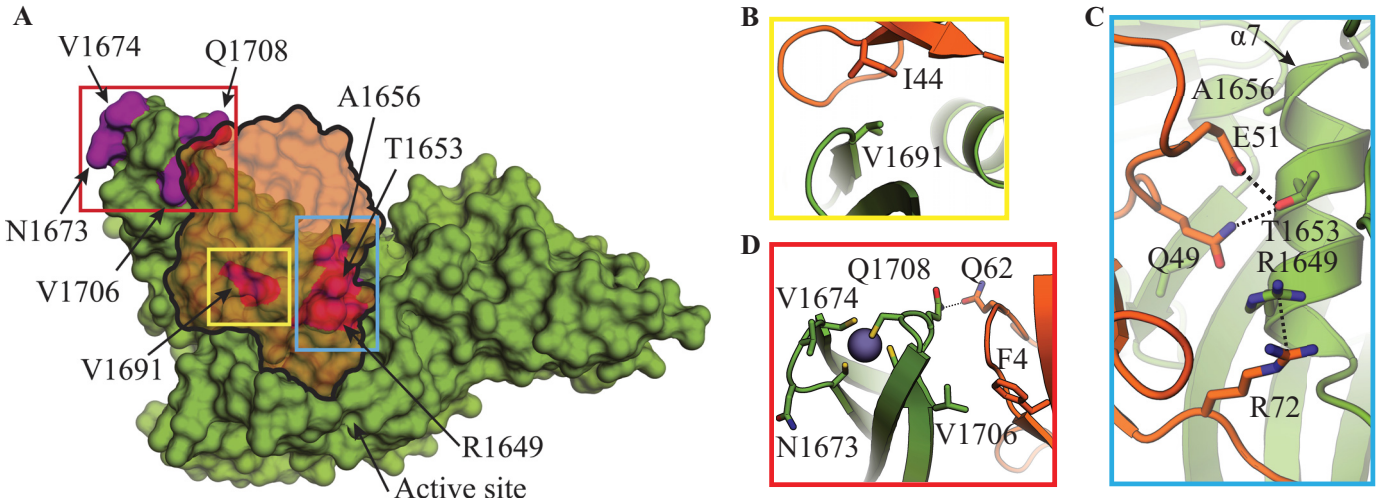

FIGURE 6. **Structure-guided mutagenesis of PL^{pro} residues involved in Ub recognition.** *A*, *surface representation* of the closed MERS-CoV PL^{pro}·Ub complex. PL^{pro} is shown in *green*, and Ub is shown in *transparent orange*. Those residues that were mutated in order to disrupt Ub binding are *colored magenta* and are indicated with *arrows*. *Colored boxes* refer *to close-up views* of the PL^{pro}·Ub interactions and are shown to the *right*. *B*, hydrophobic interaction is shown between Val^{1691} of PL^{pro} and Ile^{44} of Ub. *C*, Thr^{1653} of PL^{pro} is shown hydrogen-bonded to Gln^{49} and Glu^{51} of Ub, and Arg^{1649} of PL^{pro} is shown interacting with Arg^{72} of Ub. *D*, hydrogen-bonding interactions are shown between Gln^{1708} of PL^{pro} and Gln^{62} of Ub, and a hydrophobic interaction is shown between Val^{1706} of PL^{pro} and Phe^{4} of Ub. Asn^{1673} and Val^{1674} of PL^{pro}, which do not interact with Ub, are also displayed. Images were created using PyMOL (70).

were found to occur in this complex (Fig. 6*D*). Residue Ala^{1656} is positioned near the C terminus of PL^{pro} helix α7, and although it is not directly involved in Ub binding, we believed that it was positioned such that the introduction of larger residues (*e.g.* arginine or phenylalanine) could disrupt Ub recognition, and thus this residue was targeted for mutation (Fig. 6*C*). Two residues on the solvent-facing region of the PL^{pro} zinc ribbon motif, Asn^{1673} and Val^{1674}, were also targeted for mutagenesis. Although they do not bind Ub at the S1 binding site (the substrate binding site on PL^{pro} responsible for binding mono(Ub) in our structure; see Ref. 64 for nomenclature), we hypothesized that it may inhibit association with the distal Ub on Lys^{63} poly-Ub chains based on a superposition of a Lys^{63}-linked di-Ub model onto the PL^{pro}-bound Ub molecule of the closed PL^{pro}·Ub complex structure determined here (not shown). In addition, the crystal structure of USP21 bound to linear di-Ub was recently determined and revealed that the tip of the fingers domain of this DUB acts as an S2 recognition site, binding to the distal Ub of a linear di-Ub molecule (57). Given the structural similarity between Lys^{63} di-Ub and linear di-Ub and the clear activity we observed for MERS-CoV PL^{pro} toward Lys^{63}, we hypothesized that mutating residues Asn^{1673} and Val^{1674} near the zinc ribbon may also disrupt Ub processing.

Targeted Mutations within the PL^{pro}·Ub Binding Site Disrupt Ub Processing but Not Proteolytic Cleavage of the nsp3 ↓ 4 Site

Using a previously described ectopic expression assay (61), we monitored the effects of amino acid substitutions in PL^{pro}, as described above, on overall levels of Ub-conjugated proteins in HEK293T cells as well as the ability of these PL^{pro} variants to process the MERS-CoV nsp3 ↓ 4 polyprotein cleavage site *in trans*. V5-tagged PL^{pro} (wild type and mutants) was co-expressed with N-terminally HA-tagged and C-terminally V5-tagged MERS-CoV nsp3C-4 excluding the PL^{pro} domain, hereafter referred to as HA-nsp3C-4-V5. We assume that the successful processing of the nsp3 ↓ 4 site in HA-nsp3C-4-V5 is indicative of unaltered proteolytic cleavage capability of PL^{pro}, which during infection facilitates the release of nsp1, -2, and -3 from the viral polyproteins. Processing of HA-nsp3C-4-V5 in *trans* by wild-type PL^{pro} and our panel of mutants was visualized via Western blotting (Fig. 7*A*). Whereas wild-type PL^{pro} was able to cleave HA-nsp3C-4-V5 substrate in *trans*, the PL^{pro} active site mutant C1592A was unable to cleave the nsp3 ↓ 4 site (Fig. 7*A*, compare *lanes 5* and *6* and *lanes 19* and *20*). As expected, each of the substitutions in the Ub-binding site of PL^{pro} only minimally affected nsp3 ↓ 4 cleavage, with the exception of the A1656R mutant that displayed a clearly reduced ability to cleave HA-nsp3C-4-V5 compared with wild-type PL^{pro} (Fig. 7*A*, compare *lanes 5* and *10*). This suggests that Ala^{1656} of PL^{pro} may be involved in recognizing and binding sequences in the vicinity of the nsp3 ↓ 4 cleavage site. Most double and triple substitutions tested were also slightly less efficient in cleaving HA-nsp3C-4-V5 compared with the wild-type control.

In order to analyze the effect of the mutations on overall DUB activity, PL^{pro}-V5 was co-expressed with FLAG-Ub, and the levels of FLAG-Ub-conjugated cellular proteins were visualized via Western blotting (Fig. 7*B*). Expression of wild-type PL^{pro} resulted in a strong decrease of the accumulation of FLAG-Ub conjugates, whereas a negligible effect was observed upon expression of active site mutant C1592A (Fig. 7*B*, compare *lanes 3* and *4* and *lanes 16* and *17*). Substitutions of residue Val^{1691}, positioned on strand β12 of PL^{pro}, and Thr^{1653} and Ala^{1656}, residues located on helix α7 (Fig. 6, *B* and *C*), displayed the clearest reduction of PL^{pro} DUB activity (Fig. 7*B*, *lanes 5–8*). The V1691R mutation had the most pronounced effect, and a PL^{pro} T1653R/V1691R double mutant also displayed severely reduced DUB activity, comparable with that seen for the active site mutant (Fig. 7*B*, compare *lanes 4* and *5* and *lanes 17* and *22*). Notably, a more conservative substitution at the

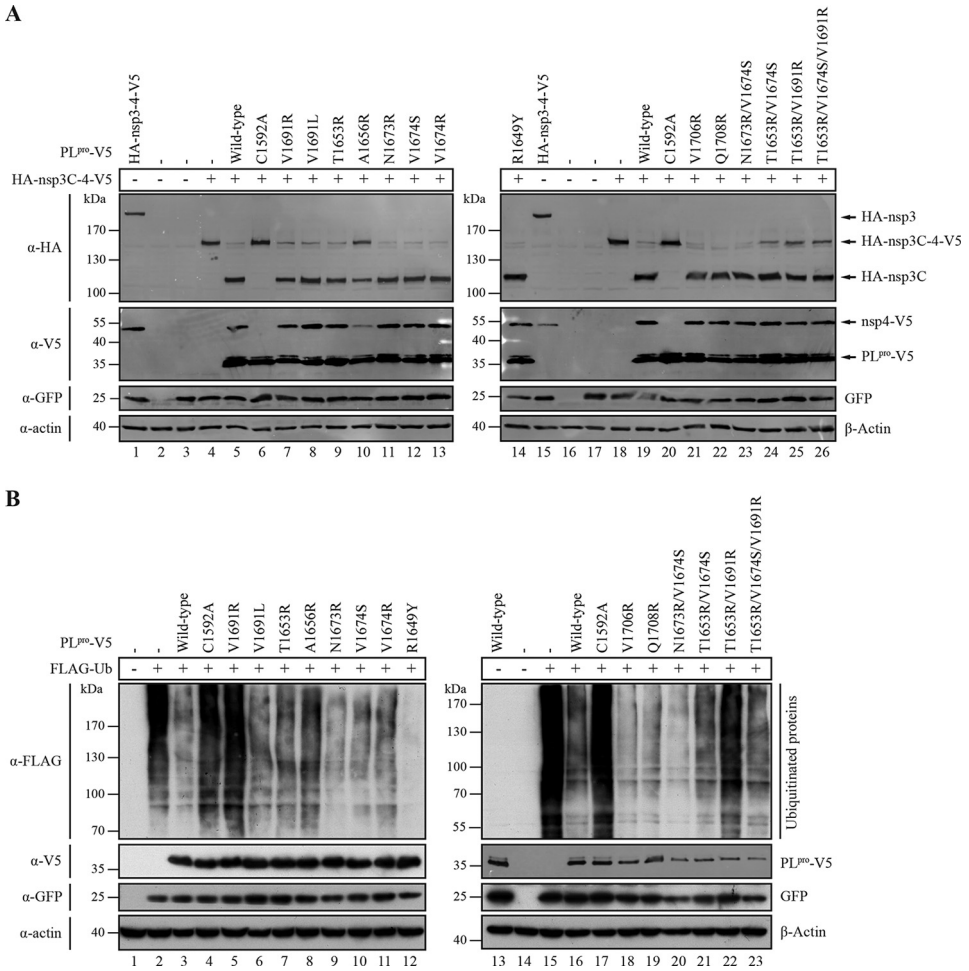

FIGURE 7. **Effect of PL^{pro} mutations on in *trans* cleavage of nsp3 ↓ 4 and on DUB activity.** *A*, HEK293T cells were co-transfected with plasmids encoding HA-nsp3C-4-V5 (which does not contain PL^{pro}), PL^{pro}-V5 (wild type and mutants), and GFP (as a transfection control). As a control, plasmid encoding HA-nsp3-4-V5, which includes the PL^{pro} domain, was transfected (*lanes 1* and *15*), and cleavage resulted in the generation of full-length HA-tagged nsp3 and V5-tagged nsp4. Cells were lysed 18 h post-transfection, and expressed proteins were analyzed by Western blotting. Proteolytic cleavage was measured from the generation of N-terminal HA-tagged nsp3C and C-terminal V5-tagged nsp4. *B*, HEK293T cells were transfected with a combination of plasmids encoding FLAG-Ub, PL^{pro}-V5 (wild-type and mutants), and GFP (as a transfection control). Cells were lysed 18 h post-transfection, and expressed proteins were analyzed by Western blotting to visualize the deconjugation of FLAG-tagged Ub from a wide range of cellular proteins by MERS-CoV PL^{pro} wild-type and mutants.

same position, V1691L, had a much less pronounced effect on DUB activity (Fig. 7*B*, *lane 6*). Substitution of Val^{1674} with either Ser or Arg impaired DUB activity but to a much lesser extent than substitutions targeting Val^{1691}, Thr^{1653}, and Ala^{1656} (Fig. 7*B*, compare *lanes 5–8*, *10*, and *11*). The N1673R substitution did not negatively affect DUB activity of PL^{pro} at all, whereas the N1673R/V1674S double substitution resulted in slightly greater DUB activity (Fig. 7*B*, *lanes 9* and *20*). These results do not support our hypothesis based on modeling that Asn^{1673} and Val^{1674} might form part of an S2 binding site that recognizes an additional distal Ub within a Lys^{63}-linked chain. Further structural studies are needed to validate the role of these residues in binding Ub chains. It should be noted, however, that these mutants may still be able to process Lys^{63}-linked poly-Ub chains by recognizing a single Ub monomer at the end of a poly-Ub substrate, which may explain the ineffectiveness of these mutations in disrupting DUB activity. Mutations at residues Val^{1706} and Gln^{1708} did not influence DUB activity of PL^{pro} (Fig. 7*B*, *lanes 18* and *19*). Given that these residues were only found to interact with Ub in our closed PL^{pro} structure (Fig. 6*A*), their failure to inhibit DUB activity in this cellular DUB assay is not surprising and indicates that these residues are not essential for Ub recognition. Interestingly and repeatedly observed, the R1649Y mutant was found to have even greater DUB activity than wild-type PL^{pro} (Fig. 7*B*, compare *lanes 3* and *12*). This residue was found to interact with residue Arg^{72} of Ub, and although this result was unexpected, it is possible that the R1649Y mutant retains the ability to interact with Arg^{72} of Ub via a cation-π interaction between the aromatic tyrosine inserted into PL^{pro} and the positively charged arginine of Ub. Together, the findings from our mutagenesis study demonstrate that it is possible to selectively decouple the DUB and polyprotein processing activities of MERS-CoV PL^{pro} through structure-guided site-directed mutagenesis.

PL^{pro} DUB Activity Suppresses the Innate Immune Response

Conjugation and deconjugation of Ub plays an important role in the regulation of the innate immune response, and not surprisingly, pathogens have evolved mechanisms to subvert these Ub-

dependent pathways (reviewed in Ref. 22). For arteriviruses, which are distant relatives of CoVs within the nidovirus order, it has been shown that the DUB activity of their PLP2 is involved in antagonizing IFN-β activation upon ectopic expression, and for equine arteritis virus, this was confirmed during infection in host cells (61, 65). Coronavirus papain-like proteases have been suggested to act as IFN-β and NF-κB antagonists as well (15, 23, 66, 67). MERS-CoV PL^{pro} is thought to possess these properties based on its capability to inhibit RIG-I-, MDA5-, and MAVS-induced IFN-β promoter stimulation and to reduce TNF-α-induced NF-κB reporter gene activity (9, 16). We therefore designed luciferase-based reporter gene assays to establish whether the DUB activity of MERS-CoV PL^{pro} alone suffices to antagonize the IFN-β pathway. To this end, we first assessed at which level of this innate immune signal transduction pathway MERS-CoV PL^{pro} is most active as a suppressor.

Innate immune signaling was induced in HEK293T cells by expression of one of three signaling factors, RIG-I, MAVS, or IRF3, which stimulate the pathway leading to IFN-β production at different levels. Because RIG-I and IRF3 normally need to be activated through post-translational modification (ubiquitination and phosphorylation, respectively), constitutively active variants were used (RIG-I$_{(2CARD)}$ and IRF3$_{(5D)}$), which efficiently induce downstream signaling independent of these activation steps. Cells were co-transfected with plasmids encoding one of these innate immune signaling proteins and wild-type PL^{pro}, the PL^{pro} active site mutant C1592A, or full-length MERS-CoV nsp3 containing the PL^{pro} domain. The inhibitory effect of the PL^{pro} variants on the activation of the IFN-β promotor by the different stimuli was measured via co-expression of a firefly luciferase reporter gene under control of the IFN-β promoter. Another co-transfected plasmid encoding *Renilla* luciferase was included as an internal control in order to be able to correct for variability in transfection efficiency. At 16 h post-transfection, luciferase activities were measured, and activation of the IFN-β promoter induced by expression of RIG-I$_{(2CARD)}$, MAVS, or IRF3$_{(5D)}$ was set at 100% (Fig. 8). In accordance with Mielech *et al.* (16), we observed that MERS-CoV PL^{pro} significantly reduced the IFN-β promoter activation that could be induced by expression of either RIG-I$_{(2CARD)}$ or MAVS. This effect was concentration-dependent, whereas the PL^{pro} active site mutant was unable to block IFN-β promoter activation (Fig. 8, *A* and *C*). MERS-CoV nsp3 expression also inhibited RIG-I- and MAVS-mediated IFN-β promoter induction (Fig. 8, *B* and *D*), and together this suggested that PL^{pro} inhibits innate immune signaling at least downstream of the MAVS adaptor and possibly also in the signaling between RIG-I and MAVS. MERS-CoV PL^{pro} also inhibited activation of the IFN-β promoter after stimulation with IRF3$_{(5D)}$ in a concentration-dependent manner, whereas the C1592A mutant did not reduce IFN-β promoter activation (Fig. 8*E*). However, expression of full-length MERS-CoV nsp3 did not significantly inhibit IFN-β promoter activation after stimulation with IRF3$_{(5D)}$ (Fig. 8*F*). This suggests that the subcellular localization of the protease, which in the case of full-length nsp3 is membrane-anchored and in the case of the PL^{pro} domain is presumably cytosolic, may be important in determining its substrate specificity. Taken together, our results suggest that MERS-CoV PL^{pro} primarily interferes with the IFN-β signaling pathway at the level between MAVS and IRF3.

We therefore chose to use MAVS-mediated induction of IFN-β promoter activation in subsequent experiments. This also resulted in the strongest inhibition by PL^{pro}, providing a maximum window to assess the effects on IFN-β promoter inhibition by the PL^{pro} mutants with specifically inactivated DUB activity. Inhibition of IFN-β promoter activation by wild-type and mutant PL^{pro} was determined by calculating the relative luciferase activity (Fig. 9). Expression of wild-type PL^{pro} reduced MAVS-induced IFN-β promoter activity to ~20% of the control, whereas active site mutant C1592A reduced it by only a few percent compared with the untreated control (Fig. 9). Substitutions T1653R and A1656R resulted in greatly impaired DUB activity (Fig. 7*B*, *lanes 7* and *8*), and compared with wild-type PL^{pro}, expression of these mutants resulted in higher IFN-β promoter activity, with relative luciferase values of ~54 and 58% respectively (Fig. 9). It should, however, be noted that the A1656R mutant was also impaired in cleaving the nsp3 ↓ 4 site, and therefore this mutation nonspecifically disrupted the two proteolytic functions of PL^{pro}. Strikingly, each mutant containing the V1691R substitution was completely unable to inhibit IFN-β promoter activation, resulting in relative luciferase activity levels similar to those seen with the active site mutant (Fig. 9, *lanes 4*, *16*, and *17*). This strongly suggested that the DUB activity of PL^{pro}, which we found to be severely impaired in V1691R mutants (Fig. 7*B*), is responsible for suppressing MAVS-induced IFN-β promoter activity in this assay. The level of reduction in DUB activity corresponded to the degree of inhibition of IFN-β promoter activation for all PL^{pro} mutants tested, which strengthens this conclusion. In accordance with its increased DUB activity, mutant R1649Y suppressed MAVS-induced IFN-β promoter activity more effectively than wild-type PL^{pro}.

Taken together, our data show that the DUB activity of MERS-CoV PL^{pro} suffices to efficiently suppress MAVS-induced IFN-β promoter activation and that this activity can be selectively disabled, without disrupting protease activity toward the nsp3 ↓ 4 cleavage site, by targeting the Ub-binding site of the enzyme. This demonstrates for the first time that the DUB activity of MERS-CoV PL^{pro} is specifically responsible for suppressing the innate immune response.

DISCUSSION

Guided by the MERS PL^{pro}·Ub crystal structures, we here describe how the DUB activity of PL^{pro} can be selectively disabled by introducing mutations into the S1 binding pocket of the protease (Fig. 6). Particularly, the substitution of Val^{1691} with the bulky and charged arginine residue severely impaired DUB activity in our cell culture-based assays. In addition, our results demonstrate that the majority of the mutations within the S1 Ub-binding site of PL^{pro} that were tested do not affect *trans* cleavage of the nsp3 ↓ 4 junction, with the exception of an A1656R mutant that did disrupt cleavage of the nsp3 ↓ 4 site. The latter result indicates that Ala^{1656} resides in a region of PL^{pro} that recognizes both Ub and a region of the nsp3C-4 construct that was used to test cleavage efficiency.

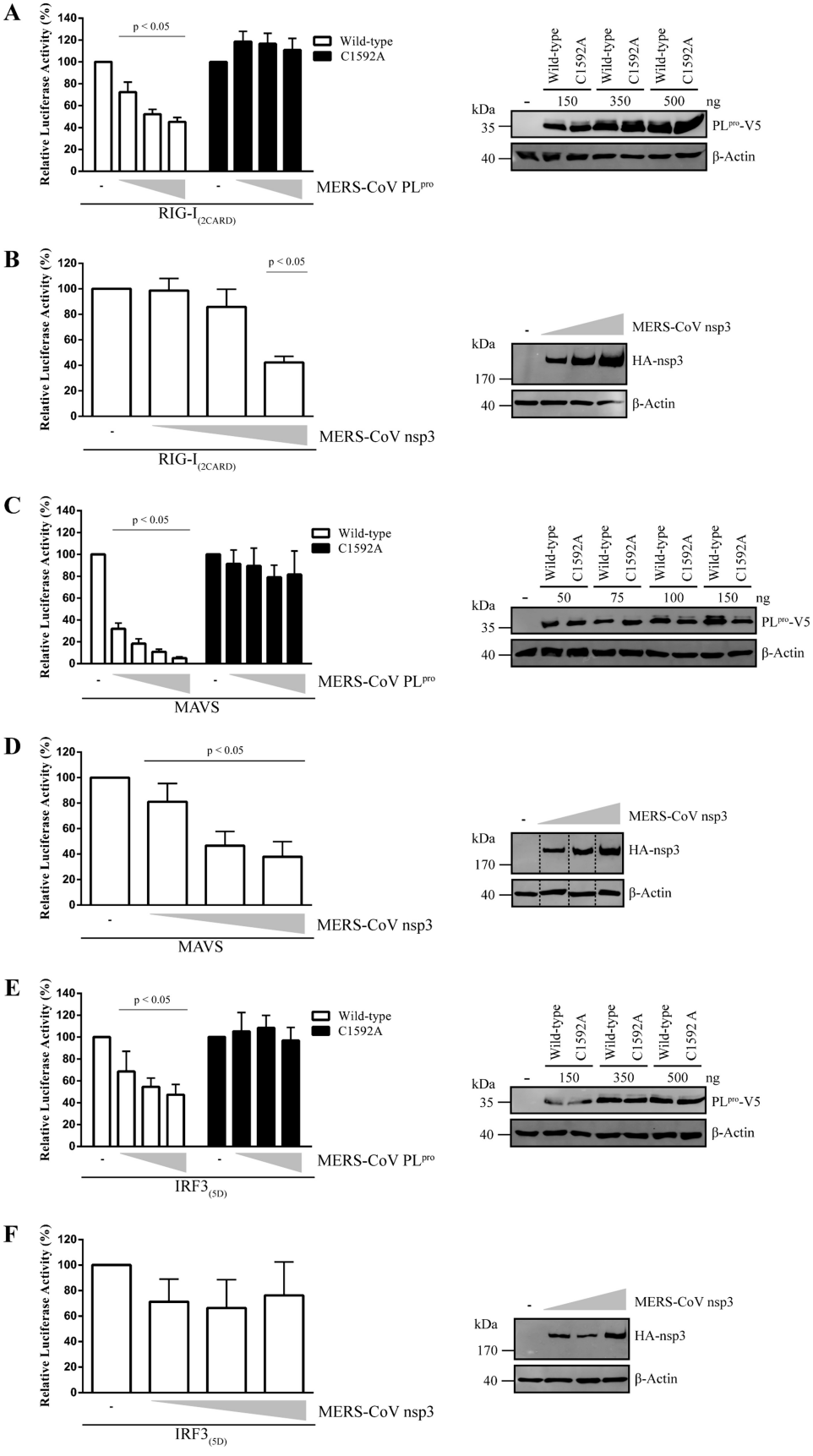
A
Relative Luciferase Activity (%)
p < 0.05
Wild-type
C1592A
MERS-CoV PLpro
RIG-I(2CARD)
Wild-type
C1592A
ng
150
350
500
kDa
35
40
PLpro-V5
β-Actin
B
p < 0.05
MERS-CoV nsp3
RIG-I(2CARD)
170
HA-nsp3
C
p < 0.05
MAVS
50
75
100
150
D
p < 0.05
MERS-CoV nsp3
MAVS
E
p < 0.05
MERS-CoV PLpro
IRF3(5D)
F
MERS-CoV nsp3
IRF3(5D)

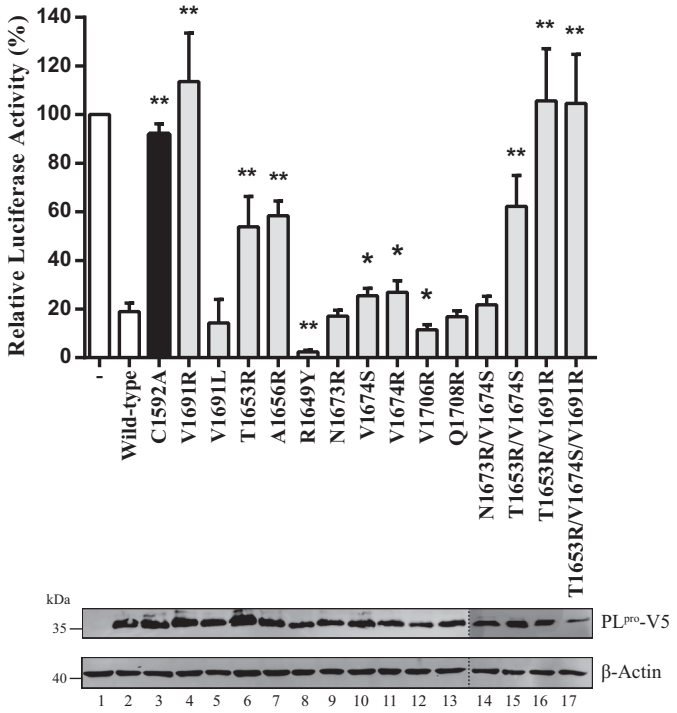

FIGURE 9. **DUB activity is required for IFN-β promoter antagonism by MERS-CoV PL^{pro}.** HEK293T cells were transfected with plasmids encoding a firefly luciferase reporter gene under control of the IFN-β promoter, *Renilla* luciferase, innate immune response inducer MAVS (25 ng), and MERS-CoV PL^{pro} wild type and mutants (75 ng). At 16 h post-transfection, cells were lysed, and luciferase activity was measured. All experiments were repeated independently at least four times. Significance relative to wild type was evaluated using an unpaired two-tailed Student's *t* test; significant values were indicated as follows: *, $p < 0.05$; **, $p < 0.01$. *Bars*, mean; *error bars*, S.D. Western blotting was used to verify expression of MERS-CoV PL^{pro}.

Our results demonstrate that the DUB activity of MERS-CoV PL^{pro} inhibits IFN-β promoter activation when innate immune signaling is induced by co-expression of either RIG-I or MAVS. The fact that suppression of IFN-β promoter activation was completely eliminated for several of our mutants (Fig. 9) strongly suggests that the proteolytic activity still present in those mutant enzymes has no additional role in the suppression of this particular branch of the innate immune response (*e.g.* by directly cleaving RIG-I or MAVS). A number of other CoV papain-like proteases with DUB activity have also been implicated in antagonizing the host innate immune response (15, 23, 66, 67). In agreement with our data, recent studies have demonstrated the ability of MERS-CoV PL^{pro} to inhibit RIG-I-, MDA5-, and MAVS-dependent IFN-β promoter activation as well as to down-regulate the level of IFN-β mRNA transcripts in MDA5-stimulated cells (16). The current data support the hypothesis that all of these activities solely depend on the deubiquitinating capacities of these coronavirus enzymes. Reports regarding the dependence of MERS-CoV PL^{pro}-mediated IFN-β antagonism on the enzyme's protease activity have, however, varied thus far. Mielech *et al.* (16) recently demonstrated that a MERS-CoV nsp3 fragment containing PL^{pro} but excluding the transmembrane domain can inhibit MAVS-, RIG-I-, and MDA5-dependent IFN-β promoter activation, and MDA5 mediated IFN-β mRNA transcription only with a functional PL^{pro} active site. Yang *et al.* (9) on the other hand used a MERS-CoV PL^{pro} expression product extending into the nsp3 transmembrane region to demonstrate that down-regulation of RIG-I-stimulated IFN-β promoter activity is seen even with an active site knock-out mutant. Here we show that inhibition of RIG-I-, MAVS-, and IRF3-induced IFN-β promoter activity by the MERS-CoV PL^{pro} domain is clearly dependent on a functional active site and that it is specifically the DUB activity of the protease that mediates this inhibition. However, the possibility cannot be ruled out that other parts of nsp3 contain additional innate immune suppressing activities, which may be responsible for the protease-independent effects reported with longer expression products.

Ubiquitination plays an important role in the regulation of pathways involved in detecting and counteracting viral infections, and, not surprisingly, a number of viruses of substantial diversity have been found to deploy DUBs that manipulate these signaling processes by reversing the post-translational modification of cellular proteins by Ub conjugation (19, 68). Some of these DUBs, specifically those found in (+)RNA viruses, are also critical for viral replication by catalyzing the proteolytic cleavage of specific sites in viral polyproteins, thus complicating our ability to study the direct effects of the additional DUB activity of these viral proteases. Ultimately, these effects need to be studied in the context of a viral infection; however, a simple inactivation of the protease/DUB would not only fail to prove the specific involvement of the DUB activity, it would also prevent viral replication. The method described here selectively removed the DUB activity of the MERS-CoV PL^{pro} domain while leaving polyprotein processing activity at the nsp3 ↓ 4 site unhindered, thus paving the way for the application of these mutations to recombinant MERS-CoV and the direct study of the role of DUB activity during infection.

We were able to show that Lys^{48}- and Lys^{63}-linked poly-Ub chains are processed *in vitro* by MERS-CoV PL^{pro} at similar rates, which is in accordance with a recent report by Báez-Santos *et al.* (50). In contrast, SARS-CoV PL^{pro} rapidly cleaves Lys^{48}-linked poly-Ub and displays only moderate activity for Lys^{63} linkages in similar assays (62). It has been suggested that SARS-CoV PL^{pro} may recognize Lys^{48}-linked di-Ub via its S1 and S2 sites (62), although to date, no crystal structures have been reported of SARS-CoV PL^{pro} in complex with a di-Ub substrate. Similarly, no such structural data have been obtained

FIGURE 8. **MERS-CoV PL^{pro} inhibits RIG-I- and MAVS-induced IFN-β promoter activity.** HEK293T cells were transfected with a combination of plasmids expressing a firefly luciferase reporter gene under control of the IFN-β promoter, *Renilla* luciferase; innate immune response inducers RIG-I$_{(2CARD)}$, MAVS, or IRF3$_{(5D)}$; and increasing amounts of MERS-CoV PL^{pro} wild-type, active site mutant C1592A (*A*, *C*, and *E*), or full-length MERS-CoV nsp3 (*B*, *D*, and *F*). Upon induction of the innate immune response with RIG-I$_{(2CARD)}$ and IRF3$_{(5D)}$, cells were transfected with the PL^{pro} (0, 150, 350, or 500 ng) or nsp3 (0, 350, 500, of 1000 ng) constructs. Upon induction with MAVS, cells were transfected with the PL^{pro} (0, 50, 75, 100 or 150 ng) or nsp3 (0, 150, 350 or 500 ng) constructs. At 16 h post-transfection, cells were lysed, and luciferase activity was measured. All experiments were repeated independently at least four times. Significance was evaluated using an unpaired two-tailed Student's *t* test; *p* values of <0.05 were considered significant. *Bars*, mean; *error bars*, S.D. Western blotting was used to verify expression of MERS-CoV PL^{pro} and nsp3.

for MERS-CoV PL^{pro}, and thus future structural studies are necessary to determine precisely how MERS-CoV PL^{pro} recognizes poly-Ub substrates and whether the preferences observed in expression systems can be confirmed in situations representative of an infection.

In addition to deconjugating Ub, MERS- and SARS-CoV PL^{pro} also recognize the antiviral Ubl molecule ISG15 (16, 17). In the absence of a crystal structure of a DUB from the USP family in complex with ISG15, it is difficult to predict which regions of PL^{pro} may be specifically responsible for ISG15 binding. However, it is interesting to note that both the palm and fingers domains of the SARS-CoV PL^{pro} domain (62) and the cellular USP21 (57), respectively, have been implicated in ISG15 recognition, probably through additional interactions between PL^{pro} and the N-terminal Ubl fold of ISG15. Future structural work is necessary to identify the specific determinants of ISG15 recognition by MERS-CoV PL^{pro}. Structure-guided mutagenesis of MERS-CoV PL^{pro} to selectively disrupt deISGylation without affecting polyprotein cleavage would further expand our insights into the role of this additional activity in coronaviral immune evasion. The specific removal of DUB and potentially deISGylating activity from viral proteases that suppress the host innate immune response may open new avenues to engineer attenuated viruses for use as modified-live virus vaccines.

Acknowledgments—We are grateful to Diede Oudshoorn for generating MERS-CoV nsp3-4 expression constructs and Kathleen C. Lehmann for excellent technical assistance. We kindly thank the following people for providing reagents: John Hiscott, Craig E. Cameron, Michaela U. Gack, and Adolfo García-Sastre. We thank Veronica Larmour for technical assistance and Shaun Labiuk and the staff of the Canadian Light Source (CLS) beamline 08B1-1 for assistance with data collection. The CLS is supported by the Natural Sciences and Engineering Research Council of Canada, the National Research Council, the Canadian Institutes of Health Research, and the University of Saskatchewan.

REFERENCES

1. Zaki, A. M., van Boheemen, S., Bestebroer, T. M., Osterhaus, A. D. M. E., and Fouchier, R. A. M. (2012) Isolation of a novel coronavirus from a man with pneumonia in Saudi Arabia. *N. Engl. J. Med.* **367,** 1814–1820
2. World Health Organization (2014) *Middle East Respiratory Syndrome Coronavirus (MERS-CoV): Update (United Arab Emirates)*. World Health Organization, Geneva
3. World Health Organization (2003) *Summary of Probable SARS Cases with Onset of Illness from 1 November 2002 to 31 July 2003*. World Health Organization, Geneva
4. Azhar, E. I., El-Kafrawy, S. A., Farraj, S. A., Hassan, A. M., Al-Saeed, M. S., Hashem, A. M., and Madani, T. A. (2014) Evidence for camel-to-human transmission of MERS coronavirus. *N. Engl. J. Med.* **370,** 2499–2505
5. Reusken, C. B., Farag, E. A., Jonges, M., Godeke, G. J., El-Sayed, A. M., Pas, S. D., Raj, V. S., Mohran, K. J., Moussa, H. A., Ghobashy, H., Alhajri, F., Ibrahim, A. K., Bosch, B. J., Pasha, S. K., Al-Romaihi, H. E., Al-Thani, M., Al-Marri, S. A., AlHajri, M. M., Haagmans, B. L., and Koopmans, M. P. (2014) Middle East respiratory syndrome coronavirus (MERS-CoV) RNA and neutralising antibodies in milk collected according to local customs from dromedary camels, Qatar, April 2014. *Euro Surveill.* **19,** 20829
6. van Boheemen, S., de Graaf, M., Lauber, C., Bestebroer, T. M., Raj, V. S., Zaki, A. M., Osterhaus, A. D., Haagmans, B. L., Gorbalenya, A. E., Snijder, E. J., and Fouchier, R. A. (2012) Genomic characterization of a newly discovered coronavirus associated with acute respiratory distress syndrome in humans. *MBio* 10.1128/mBio.00473–12
7. Firth, A. E., and Brierley, I. (2012) Non-canonical translation in RNA viruses. *J. Gen. Virol.* **93,** 1385–1409
8. Perlman, S., and Netland, J. (2009) Coronaviruses post-SARS: update on replication and pathogenesis. *Nat. Rev. Microbiol.* **7,** 439–450
9. Yang, X., Chen, X., Bian, G., Tu, J., Xing, Y., Wang, Y., and Chen, Z. (2014) Proteolytic processing, deubiquitinase and interferon antagonist activities of Middle East respiratory syndrome coronavirus papain-like protease. *J. Gen. Virol.* **95,** 614–626
10. Kilianski, A., Mielech, A. M., Deng, X., and Baker, S. C. (2013) Assessing activity and inhibition of Middle East respiratory syndrome coronavirus papain-like and 3C-like proteases using luciferase-based biosensors. *J. Virol.* **87,** 11955–11962
11. Komander, D., and Rape, M. (2012) The ubiquitin code. *Annu. Rev. Biochem.* **81,** 203–229
12. Komander, D., Clague, M. J., and Urbé, S. (2009) Breaking the chains: structure and function of the deubiquitinases. *Nat. Rev. Mol. Cell Biol.* **10,** 550–563
13. Frieman, M., Ratia, K., Johnston, R. E., Mesecar, A. D., and Baric, R. S. (2009) Severe acute respiratory syndrome coronavirus papain-like protease ubiquitin-like domain and catalytic domain regulate antagonism of IRF3 and NF-κB signaling. *J. Virol.* **83,** 6689–6705
14. Barretto, N., Jukneliene, D., Ratia, K., Chen, Z., Mesecar, A. D., and Baker, S. C. (2005) The papain-like protease of severe acute respiratory syndrome coronavirus has deubiquitinating activity. *J. Virol.* **79,** 15189–15198
15. Clementz, M. A., Chen, Z., Banach, B. S., Wang, Y., Sun, L., Ratia, K., Baez-Santos, Y. M., Wang, J., Takayama, J., Ghosh, A. K., Li, K., Mesecar, A. D., and Baker, S. C. (2010) Deubiquitinating and interferon antagonism activities of coronavirus papain-like proteases. *J. Virol.* **84,** 4619–4629
16. Mielech, A. M., Kilianski, A., Baez-Santos, Y. M., Mesecar, A. D., and Baker, S. C. (2014) MERS-CoV papain-like protease has deISGylating and deubiquitinating activities. *Virology* **450**, 64–70
17. Lindner, H. A., Fotouhi-Ardakani, N., Lytvyn, V., Lachance, P., Sulea, T., and Ménard, R. (2005) The papain-like protease from the severe acute respiratory syndrome coronavirus is a deubiquitinating enzyme. *J. Virol.* **79,** 15199–15208
18. Lindner, H. A., Lytvyn, V., Qi, H., Lachance, P., Ziomek, E., and Ménard, R. (2007) Selectivity in ISG15 and ubiquitin recognition by the SARS coronavirus papain-like protease. *Arch. Biochem. Biophys.* **466,** 8–14
19. Mielech, A. M., Chen, Y., Mesecar, A. D., and Baker, S. C. (2014) Nidovirus papain-like proteases: Multifunctional enzymes with protease, deubiquitinating and deISGylating activities. *Virus Res.* 10.1016/j.virusres.2014.01.025
20. Jensen, S., and Thomsen, A. R. (2012) Sensing of RNA viruses: a review of innate immune receptors involved in recognizing RNA virus invasion. *J. Virol.* **86,** 2900–2910
21. Goubau, D., Schlee, M., Deddouche, S., Pruijssers, A. J., Zillinger, T., Goldeck, M., Schuberth, C., Van der Veen, A. G., Fujimura, T., Rehwinkel, J., Iskarpatyoti, J. A., Barchet, W., Ludwig, J., Dermody, T. S., Hartmann, G., and Sousa, C. R. (2014) Antiviral immunity via RIG-I-mediated recognition of RNA bearing 5′-diphosphates. *Nature* 10.1038/nature13590
22. Jiang, X., and Chen, Z. J. (2012) The role of ubiquitylation in immune defence and pathogen evasion. *Nat. Rev. Immunol.* **12,** 35–48
23. Devaraj, S. G., Wang, N., Chen, Z., Chen, Z., Tseng, M., Barretto, N., Lin, R., Peters, C. J., Tseng, C.-T. K., Baker, S. C., and Li, K. (2007) Regulation of IRF-3-dependent innate immunity by the papain-like protease domain of the severe acute respiratory syndrome coronavirus. *J. Biol. Chem.* **282,** 32208–32221
24. Spiegel, M., Pichlmair, A., Martínez-Sobrido, L., Cros, J., García-Sastre, A., Haller, O., and Weber, F. (2005) Inhibition of β interferon induction by severe acute respiratory syndrome coronavirus suggests a two-step model for activation of interferon regulatory factor 3. *J. Virol.* **79,** 2079–2086
25. Spiegel, M., and Weber, F. (2006) Inhibition of cytokine gene expression and induction of chemokine genes in non-lymphatic cells infected with SARS coronavirus. *Virol. J.* **3,** 17–17
26. Cheung, C. Y., Poon, L. L. M., Ng, I. H. Y., Luk, W., Sia, S.-F., Wu, M. H. S., Chan, K.-H., Yuen, K.-Y., Gordon, S., Guan, Y., and Peiris, J. S. M. (2005) Cytokine responses in severe acute respiratory syndrome coronavirus-

infected macrophages *in vitro*: possible relevance to pathogenesis. *J. Virol.* **79,** 7819–7826
27. Chu, H., Zhou, J., Ho-Yin Wong, B., Li, C., Cheng, Z.-S., Lin, X., Kwok-Man Poon, V., Sun, T., Choi-Yi Lau, C., Fuk-Woo Chan, J., Kai-Wang To, K., Chan, K.-H., Lu, L., Zheng, B.-J., and Yuen, K.-Y. (2014) Productive replication of Middle East respiratory syndrome coronavirus in monocyte-derived dendritic cells modulates innate immune response. *Virology* **454**, 197–205
28. Chan, R. W. Y., Chan, M. C. W., Agnihothram, S., Chan, L. L. Y., Kuok, D. I. T., Fong, J. H. M., Guan, Y., Poon, L. L. M., Baric, R. S., Nicholls, J. M., and Peiris, J. S. M. (2013) Tropism of and innate immune responses to the novel human betacoronavirus lineage C virus in human *ex vivo* respiratory organ cultures. *J. Virol.* **87,** 6604–6614
29. Lau, S. K., Lau, C. C., Chan, K. H., Li, C. P., Chen, H., Jin, D. Y., Chan, J. F., Woo, P. C., and Yuen, K. Y. (2013) Delayed induction of proinflammatory cytokines and suppression of innate antiviral response by the novel Middle East respiratory syndrome coronavirus: implications for pathogenesis and treatment. *J. Gen. Virol.* **94,** 2679–2690
30. van Kasteren, P. B., Beugeling, C., Ninaber, D. K., Frias-Staheli, N., van Boheemen, S., García-Sastre, A., Snijder, E. J., and Kikkert, M. (2012) Arterivirus and nairovirus ovarian tumor domain-containing Deubiquitinases target activated RIG-I to control innate immune signaling. *J. Virol.* **86,** 773–785
31. te Velthuis, A. J., Arnold, J. J., Cameron, C. E., van den Worm, S. H., and Snijder, E. J. (2010) The RNA polymerase activity of SARS-coronavirus nsp12 is primer dependent. *Nucleic Acids Res.* **38,** 203–214
32. Gack, M. U., Albrecht, R. A., Urano, T., Inn, K. S., Huang, I. C., Carnero, E., Farzan, M., Inoue, S., Jung, J. U., and García-Sastre, A. (2009) Influenza A virus NS1 targets the ubiquitin ligase TRIM25 to evade recognition by the host viral RNA sensor RIG-I. *Cell Host Microbe* **5,** 439–449
33. Fitzgerald, K. A., McWhirter, S. M., Faia, K. L., Rowe, D. C., Latz, E., Golenbock, D. T., Coyle, A. J., Liao, S. M., and Maniatis, T. (2003) IKKε and TBK1 are essential components of the IRF3 signaling pathway. *Nat. Immunol.* **4,** 491–496
34. Gack, M. U., Shin, Y. C., Joo, C. H., Urano, T., Liang, C., Sun, L., Takeuchi, O., Akira, S., Chen, Z., Inoue, S., and Jung, J. U. (2007) TRIM25 RING-finger E3 ubiquitin ligase is essential for RIG-I-mediated antiviral activity. *Nature* **446,** 916–920
35. Seth, R. B., Sun, L., Ea, C. K., and Chen, Z. J. (2005) Identification and characterization of MAVS, a mitochondrial antiviral signaling protein that activates NF-κB and IRF 3. *Cell* **122,** 669–682
36. Lin, R., Heylbroeck, C., Pitha, P. M., and Hiscott, J. (1998) Virus-dependent phosphorylation of the IRF-3 transcription factor regulates nuclear translocation, transactivation potential, and proteasome-mediated degradation. *Mol. Cell Biol.* **18,** 2986–2996
37. Gohara, D. W., Ha, C. S., Kumar, S., Ghosh, B., Arnold, J. J., Wisniewski, T. J., and Cameron, C. E. (1999) Production of "authentic" poliovirus RNA-dependent RNA polymerase (3D(pol)) by ubiquitin-protease-mediated cleavage in *Escherichia coli*. *Protein Expr. Purif.* **17,** 128–138
38. Messick, T. E., Russell, N. S., Iwata, A. J., Sarachan, K. L., Shiekhattar, R., Shanks, J. R., Reyes-Turcu, F. E., Wilkinson, K. D., and Marmorstein, R. (2008) Structural basis for ubiquitin recognition by the Otu1 ovarian tumor domain protein. *J. Biol. Chem.* **283,** 11038–11049
39. Borodovsky, A., Ovaa, H., Kolli, N., Gan-Erdene, T., Wilkinson, K. D., Ploegh, H. L., and Kessler, B. M. (2002) Chemistry-based functional proteomics reveals novel members of the deubiquitinating enzyme family. *Chem. Biol.* **9,** 1149–1159
40. Kabsch, W. (2010) XDS. *Acta Crystallogr. D Biol. Crystallogr.* **66,** 125–132
41. Evans, P. (2006) Scaling and assessment of data quality. *Acta Crystallogr. D Biol. Crystallogr.* **62,** 72–82
42. Grosse-Kunstleve, R. W., and Adams, P. D. (2003) Substructure search procedures for macromolecular structures. *Acta Crystallogr. D Biol. Crystallogr.* **59,** 1966–1973
43. Terwilliger, T. C. (2000) Maximum-likelihood density modification. *Acta Crystallogr. D Biol. Crystallogr.* **56,** 965–972
44. Terwilliger, T. C., Adams, P. D., Read, R. J., McCoy, A. J., Moriarty, N. W., Grosse-Kunstleve, R. W., Afonine, P. V., Zwart, P. H., and Hung, L. W. (2009) Decision-making in structure solution using Bayesian estimates of map quality: the PHENIX AutoSol wizard. *Acta Crystallogr. D Biol. Crystallogr.* **65,** 582–601
45. Emsley, P., Lohkamp, B., Scott, W. G., and Cowtan, K. (2010) Features and development of Coot. *Acta Crystallogr. D Biol. Crystallogr.* **66,** 486–501
46. Afonine, P. V., Grosse-Kunstleve, R. W., Echols, N., Headd, J. J., Moriarty, N. W., Mustyakimov, M., Terwilliger, T. C., Urzhumtsev, A., Zwart, P. H., and Adams, P. D. (2012) Towards automated crystallographic structure refinement with phenix.refine. *Acta Crystallogr. D Biol. Crystallogr.* **68,** 352–367
47. Graham, F. L., and van der Eb, A. J. (1973) A new technique for the assay of infectivity of human adenovirus 5 DNA. *Virology* **52,** 456–467
48. Lin, M. H., Chuang, S. J., Chen, C. C., Cheng, S. C., Cheng, K. W., Lin, C. H., Sun, C. Y., and Chou, C. Y. (2014) Structural and functional characterization of MERS coronavirus papain-like protease. *J. Biomed. Sci.* **21,** 54
49. Lei, J., Mesters, J. R., Drosten, C., Anemüller, S., Ma, Q., and Hilgenfeld, R. (2014) Crystal structure of the papain-like protease of MERS coronavirus reveals unusual, potentially druggable active-site features. *Antiviral Res.* **109,** 72–82
50. Báez-Santos, Y. M., Mielech, A. M., Deng, X., Baker, S., and Mesecar, A. D. (2014) Catalytic function and substrate specificity of the PLpro domain of nsp3 from the Middle East respiratory syndrome coronavirus (MERS-CoV). *J. Virol.* **88,** 12511–12527
51. Ratia, K., Saikatendu, K. S., Santarsiero, B. D., Barretto, N., Baker, S. C., Stevens, R. C., and Mesecar, A. D. (2006) Severe acute respiratory syndrome coronavirus papain-like protease: structure of a viral deubiquitinating enzyme. *Proc. Natl. Acad. Sci. U.S.A.* **103,** 5717–5722
52. Faesen, A. C., Luna-Vargas, M. P., and Sixma, T. K. (2012) The role of UBL domains in ubiquitin-specific proteases. *Biochem. Soc. Trans.* **40,** 539–545
53. Rawlings, N. D., Waller, M., Barrett, A. J., and Bateman, A. (2014) MEROPS: the database of proteolytic enzymes, their substrates and inhibitors. *Nucleic Acids Res.* **42,** D503–D509
54. Krishna, S. S., Majumdar, I., and Grishin, N. V. (2003) Structural classification of zinc fingers: survey and summary. *Nucleic Acids Res.* **31,** 532–550
55. Wojdyla, J. A., Manolaridis, I., van Kasteren, P. B., Kikkert, M., Snijder, E. J., Gorbalenya, A. E., and Tucker, P. A. (2010) Papain-like protease 1 from transmissible gastroenteritis virus: crystal structure and enzymatic activity toward viral and cellular substrates. *J. Virol.* **84,** 10063–10073
56. Renatus, M., Parrado, S. G., D'Arcy, A., Eidhoff, U., Gerhartz, B., Hassiepen, U., Pierrat, B., Riedl, R., Vinzenz, D., Worpenberg, S., and Kroemer, M. (2006) Structural basis of ubiquitin recognition by the deubiquitinating protease USP2. *Structure* **14,** 1293–1302
57. Ye, Y., Akutsu, M., Reyes-Turcu, F., Enchev, R. I., Wilkinson, K. D., and Komander, D. (2011) Polyubiquitin binding and cross-reactivity in the USP domain deubiquitinase USP21. *EMBO Rep.* **12,** 350–357
58. Chou, C. Y., Lai, H. Y., Chen, H. Y., Cheng, S. C., Cheng, K. W., and Chou, Y. W. (2014) Structural basis for catalysis and ubiquitin recognition by the severe acute respiratory syndrome coronavirus papain-like protease. *Acta Crystallogr. D Biol. Crystallogr.* **70,** 572–581
59. Hu, M., Li, P., Song, L., Jeffrey, P. D., Chenova, T. A., Wilkinson, K. D., Cohen, R. E., and Shi, Y. (2005) Structure and mechanisms of the proteasome-associated deubiquitinating enzyme USP14. *EMBO J.* **24,** 3747–3756
60. Bailey-Elkin, B. A., van Kasteren, P. B., Snijder, E. J., Kikkert, M., and Mark, B. L. (2014) Viral OTU deubiquitinases: a structural and functional comparison. *PLoS Pathog.* **10,** e1003894
61. van Kasteren, P. B., Bailey-Elkin, B. A., James, T. W., Ninaber, D. K., Beugeling, C., Khajehpour, M., Snijder, E. J., Mark, B. L., and Kikkert, M. (2013) Deubiquitinase function of arterivirus papain-like protease 2 suppresses the innate immune response in infected host cells. *Proc. Natl. Acad. Sci. U.S.A.* **110,** E838–E847
62. Ratia, K., Kilianski, A., Baez-Santos, Y. M., Baker, S. C., and Mesecar, A. (2014) Structural basis for the ubiquitin-linkage specificity and deISGylating activity of SARS-CoV papain-like protease. *PLoS Pathog.* **10,** e1004113
63. Dikic, I., Wakatsuki, S., and Walters, K. J. (2009) Ubiquitin-binding domains: from structures to functions. *Nat. Rev. Mol. Cell Biol.* **10,** 659–671
64. Eletr, Z. M., and Wilkinson, K. D. (2014) Regulation of proteolysis by human deubiquitinating enzymes. *Biochim. Biophys. Acta* **1843,** 114–128

65. Sun, Z., Chen, Z., Lawson, S. R., and Fang, Y. (2010) The cysteine protease domain of porcine reproductive and respiratory syndrome virus nonstructural protein 2 possesses deubiquitinating and interferon antagonism functions. *J. Virol.* **84,** 7832–7846
66. Zheng, D., Chen, G., Guo, B., Cheng, G., and Tang, H. (2008) PLP2, a potent deubiquitinase from murine hepatitis virus, strongly inhibits cellular type I interferon production. *Cell Res.* **18,** 1105–1113
67. Xing, Y., Chen, J., Tu, J., Zhang, B., Chen, X., Shi, H., Baker, S. C., Feng, L., and Chen, Z. (2013) The papain-like protease of porcine epidemic diarrhea virus negatively regulates type I interferon pathway by acting as a viral deubiquitinase. *J. Gen. Virol.* **94,** 1554–1567
68. Randow, F., and Lehner, P. J. (2009) Viral avoidance and exploitation of the ubiquitin system. *Nat. Cell Biol.* **11,** 527–534
69. Hadari, T., Warms, J. V., Rose, I. A., and Hershko, A. (1992) A ubiquitin C-terminal isopeptidase that acts on polyubiquitin chains: role in protein degradation. *J. Biol. Chem.* **267,** 719–727
70. DeLano, W. L. (2010) *The PyMOL Molecular Graphics System*, version 1.3r1, Schrödinger, LLC, New York